Contents lists available at ScienceDirect

Progress in Oceanography

Maximum wave heights from global model reanalysis

Francesco Barbariol[a,*], Jean-Raymond Bidlot[b], Luigi Cavaleri[a], Mauro Sclavo[a], Jim Thomson[c], Alvise Benetazzo[a]

[a] Institute of Marine Sciences (ISMAR)-National Research Council (CNR), Venice, Italy
[b] European Centre for Medium-Range Weather Forecasts (ECMWF), Reading, UK
[c] Applied Physics Laboratory, University of Washington, Seattle, USA

ARTICLE INFO

ABSTRACT

Very large waves populate world oceans and challenge seafarers and offshore structures, but their long-term and global assessment is uneasy because of the scarcity of observations and their narrow time-coverage. Modern model reanalysis datasets with high spatio-temporal extent and resolution represent a valuable tool for this scope. In this paper, we use for the first time reanalysis datasets to provide a long-term and global statistical assessment of the maximum wave parameters, namely crest, crest-to-trough and envelope heights. In particular, we rely on the ERA-Interim directional wave spectra that are used to estimate the parameters of the probability distributions of wave maxima. To represent the customary single-point observations we use time extreme statistical models, while to account for the three-dimensional geometry and short-crestedness of stormy ocean waves, the statistical models are extended to space-time. In order to evaluate the accuracy of the reanalysis-based wave maxima estimates we verify them against buoy and stereo-video wave observations gathered in the North Pacific Ocean. We then provide the global assessment of maximum crest, crest-to-trough and envelope heights during typical and extreme conditions, showing the regions attaining the largest values, which we show are located in the mid-latitude storm belts, in particular in the North Atlantic Ocean. With respect to previous wave climate studies that focused on the significant wave height only, in this study we quantify the maximum wave height extent, also highlighting the role of mean wave steepness and kurtosis (measures of nonlinearity) and spectral bandwidth (measure of irregularity). Beside this, we show that the contribution of the short-crestedness is significant and that taking it into account may be relevant for the safety of navigation, ship routing and marine structural design.

1. Introduction

The assessment of maximum wave heights over the oceans has challenged for a long while scholars and seafarers. This is due on the one hand to the intrinsic random character of ocean waves, forcing scholars to rely mostly on statistical approaches; on the other hand to the not yet fully unveiled physical mechanisms of large wave generation. In the past decades, many attempts have been made to frame the occurrence of extreme single wave heights into theoretical models, based on, and referenced to, field observations and laboratory or numerical experiments (see Dysthe et al., 2008 for a review of the topic).

In this paper, we combine numerical wave model outputs and extreme statistics to analyse the characteristics of the maximal wave heights over the world oceans during 25 years (1992–2016). We exploit model reanalysis datasets, in particular ERA-Interim (Dee et al., 2011), to obtain a global, long-term coverage of directional wave spectra in order to derive the corresponding parameters of the short-term (i.e., at sea state scale) extreme wave height probability distributions. Then, we do a statistical analysis to infer the long-term characteristics, i.e., the climate, of maximum wave heights over the global oceans.

We rely on model data as they allow a spatial and temporal coverage wider and denser than that given by observational datasets (usually limited in time or space, or both). Previous attempts of assessing the global wave climate from model datasets can be found in Cox and Swail (2001) and Stopa and Cheung (2014a), among others. Using satellite altimeter data Young et al. (2011) have focused on the corresponding climate trends over the global oceans. While those studies investigated the distribution of the significant wave height, here, for the first time, we aim at assessing the climate features of the maximum expected crest, crest-to-trough and envelope heights of sea states, evaluated in a statistical sense as expected values.

To this end, we follow two different theoretical statistical

approaches: a first one (*time extremes*) that is appropriate to predict maximum wave heights at a single-point (e.g., as they are observed using a wave buoy), and a second one (*space-time extremes*) that is in agreement with areal observations (obtained, for instance, with a stereo video system). We present results of both these approaches. They have different domains of observation/prediction (i.e., point vs area, respectively) and different instruments for observation (e.g., buoy vs stereo imagery, respectively). They are also applied in different contexts: time extremes complying with the traditional observations and wave statistics at a fixed point; space-time extremes allowing interpreting maximum wave heights over a given area (e.g., the one of interest for a ship or an offshore platform) and accounting for the short-crestedness of wind-generated waves. We base the assessment of wave maxima upon statistical wave models (presented in details in Section 2.1 and Appendix A) widely recognized by the community and which well represent the available observations. In particular we use a linear model for the maximum (time and space-time) crest-to-trough heights, we rely on a nonlinear second order wave model for the maximum (time and space-time) crest heights and we choose a third order nonlinear model for the maximum time envelope heights (defined as twice the amplitude of the envelope maximum). In so doing, we aim at providing a comprehensive perspective on maximum wave heights, accounting for the statistical models of wave maxima renown by the scientific and engineering communities.

The paper is organized as follows. In Section 2, we present the statistical models of wave maxima, the reanalysis model datasets and the observational datasets used in this study. In Section 3, we assess the validity of the statistical models and the accuracy of model reanalyses using buoy and stereo-video observations in the North Pacific Ocean. The global long-term climate of maximum wave heights is presented in Section 4, while discussions and a focus on some stations and transects representing regions of interest in the world follow in Section 5. We summarize our conclusions in Section 6 and we close the paper with two Appendices where we provide more details on the statistical models of maxima and on the data analysis procedures we used.

2. Materials and methods

2.1. Statistical models of maximum wave heights

Given the intrinsic random character of oceanic waves, hence of their crest height C, crest-to-trough height H and envelope wave height E, to assess the corresponding maximum values over a sea state (namely, C_{max}, H_{max} and E_{max}, respectively) it is customary to rely on a statistical approach (as done, among others, by Casas-Prat and Holthuijsen (2010), Holthuijsen (2007), Janssen and Bidlot (2009)). In this context, a typical estimate of wave heights is provided by the expected (or mean) values $\overline{C}_{max}$, $\overline{H}_{max}$ and $\overline{E}_{max}$ (the overbar representing expectation), given that the respective probability distributions of maxima are known. In the following, we will briefly introduce the statistical approaches we use in this study to represent such probability distributions (further details can be found in Appendix A).

2.1.1. Time extremes

The first statistical approach we consider is based on the assumption of a time-variate sea surface elevation, as it occurs at a fixed point in space. This is the standard approach in extreme wave analysis, appropriate to interpret single-point observations (e.g., from buoy or wave probes). In this respect, given a generic short-term parent distribution of C (say H or E) at a point, the probability of the corresponding maximum value C_{max} (say H_{max} or E_{max}) during a sea state of given duration is obtained following the principles of the extreme value analysis (Goda, 2000; Gumbel, 1958). Accordingly, the expected value of maxima provides the statistical character of the assessment.

An indication about customary short-term parent distributions of C and H at a point is given by the DNV-RP-C205 Recommended Practice

for Environmental Conditions and Environmental Loads (DNV GL, 2017; henceforth, DNV-RP). The DNV-RP is a recent guideline for marine structure designers, providing guidance for modelling, analysis and prediction of environmental conditions, including maximum wave heights. According to DNV-RP, the short-term parent probability distributions of C and H are well represented respectively by the Forristall (2000) and the Naess (1985) Weibull-type distributions, whose probabilities of extremes are recognized as the standard models for C_{max} and H_{max} at a single-point (Dysthe et al., 2008) and herein adopted. In previous studies, predictions from these models were compared against single-point observations and results of numerical simulations, showing fair agreement (see e.g., Casas-Prat and Holthuijsen, 2010; Forristall, 2000).

A short-term parent probability distribution of E at a point has been proposed by Janssen (2003, 2014) relating the occurrence of envelope heights to the directional wave spectrum and its spectral parameters. This probability of maximum envelope heights is therefore herein considered as the standard model for E_{max}. This model, verified against buoy observations (Janssen and Bidlot, 2009), is implemented in the Integrated Forecasting System of the European Centre for Medium-Range Weather Forecasts (ECMWF, 2017) such that forecast and re-analysed maximum envelope heights are routinely produced by ECMWF. It is worth noting that the expected value of E_{max} is at present the only operational product of individual maximum wave height.

Therefore, in this study we will use $\overline{C}_{max,F}$, $\overline{H}_{max,Na}$ and $\overline{E}_{max,J}$ as the statistical estimate of maximum crest, crest-to-trough and envelope heights, respectively, in a sea state of duration D (the sub indexes F, Na and J representing the Forristall, Naess and Janssen distributions, respectively).

2.1.2. Space-time extremes

To account for the 3D geometry of very large waves (Benetazzo et al., 2017; Fedele et al., 2013), we consider in this study a space-time extreme model, which extends the time-variate estimate of wave maxima to space-time, i.e., to an area of given size X and Y, over a duration D. It was proven that the values of C_{max} and H_{max} over a sea surface area are generally larger than those attained at a single point within the area (Barbariol et al., 2015; Benetazzo et al., 2015; Dysthe et al., 2008; Fedele et al., 2013; Krogstad et al., 2004). This is particularly true in short-crested conditions, typical of sea storms. Space-time extreme models consider the actual sea surface elevation as a multidimensional (2D space + time) random field and relate the probability distribution of C_{max} over a certain space-time region to the probability of the global maxima of the random field (Adler, 1981; Adler and Taylor, 2007; Piterbarg, 1996). The contribution of a weakly nonlinearity can also be included (Benetazzo et al., 2015; Fedele, 2015). The H_{max} estimate is obtained by means of the Quasi-Determinism theory (Boccotti, 2000) which provides the average shape of the largest waves and, thus, couples the crest and crest-to-trough heights. Only crest and crest-to-trough heights are evaluated in space-time, as a space-time framework for envelope heights is not available at present.

Space-time extreme wave models have been assessed using space-time extreme wave data from numerical simulations (Barbariol et al., 2015; Forristall, 2006; Socquet-Juglard et al., 2005), laboratory experiments (Forristall, 2011), and field observations (Benetazzo et al., 2017a, 2017b; Fedele et al., 2013). The same models have also been successfully employed to interpret the occurrence of well-known freak wave events, such as the Draupner wave (Cavaleri et al., 2016; Cavaleri et al., 2017). For these reasons, a space-time wave model for C_{max} and H_{max} (Space-Time Quasi-Determinism, hereinafter STQD; Benetazzo et al., 2017) has been recently implemented in the WAVEWATCH III wave model (Barbariol et al., 2017; WW3DG, 2016). The STQD model herein adopted is linear (subscript 1) for crest-to-trough heights, which are only slightly affected by nonlinearities (Tayfun and Fedele, 2007), while it accounts for second order non-resonant wave nonlinearities

(subscript 2) for crest heights. In this study we will therefore estimate the expected maximum crest and crest-to-trough height over a sea state of duration D and space size XY, as $\overline{C}_{max,STQD2}$ and $\overline{H}_{max,STQD1}$, respectively.

Provided the stationarity (in time) and homogeneity (over space) requirements are fulfilled, the choice of the time duration D as well as of the space region size XY is arbitrary and it is usually driven only by the purpose of specific applications (e.g., the duration of a wave record from a buoy or the size of an off-shore platform). Here, since we are not interested in a particular application, but rather in estimating maximum wave heights over the global oceans, we choose as duration the typical buoy record length, $D = 20$ min, and as space region a typical size of an offshore platform, $XY = 100 \times 100\,\mathrm{m}^2$. These values, which are independently chosen, satisfy the requirements of homogeneity and stationarity of the sea state and, at the same time, ensure statistical significance, as the sea state contains $O(10^2)$ waves on average. Moreover, keeping the same duration D and accounting for space-time correlation (thus, eventually reducing the number of space-time waves accordingly) allows comparing time and space-time extreme results, pointing out the genuine dimensional effect arising when the space dimension is added to time. Finally, the duration of 20 min is the reference period conventionally used to define rogue wave thresholds, i.e. $1.25H_s$ for crest height and $2.00H_s$ for crest-to-trough height (DNV GL, 2017).

2.2. Numerical model data

For maximum wave height assessment, the input variable is the directional (i.e., frequency and direction) wave spectrum, which is used to estimate the parameters of the statistical distributions of time and space-time extremes (see Appendix A). We use the directional spectra provided by two wave reanalysis datasets: ERA-Interim (Dee et al., 2011), allowing global and long-term extreme wave analysis, and ERA-5 (Hersbach et al., 2018), herein used for the analysis of the local wave conditions in the North Pacific Ocean. The sensitivity of the maximum wave parameters upon errors in model spectra has been discussed by Holthuijsen (2007), who shown that the estimate of the most probable time extreme linear crest height is only slightly affected by an error in the estimate of the average number of waves (as a consequence, for instance, of errors in spectral parameters): doubling the number of waves, provided that it is large enough, the relative error is 4.3%. This condition might not hold for a small number of waves and nonlinear estimates, which chiefly depend on the spectral shape. In this context, Barbariol et al. (2017) have shown, for instance, that a 5% error in the frequency bandwidth of a JONSWAP spectrum with $\cos^2$ directional distribution leads to a 2% error in the estimate of the nonlinear crest height $\overline{C}_{max,STQD2}$. Similar considerations can be drawn for the directional spreading. Finally, as far as the effect of the model resolutions on wave maxima is concerned, it will be discussed in the Section 3, where the results from the two datasets in the overlapping period are intercompared.

2.2.1. ERA-interim

The assessment of the long-term evolution of maximum wave heights over the global oceans is based upon the ERA-Interim dataset, produced by ECMWF. ERA-Interim (henceforth, EI) is a global reanalysis which uses two-way coupled atmosphere and wave model components (within an integrated atmosphere-ocean waves-land system), the latter based on the WAM model (Komen et al., 1994). We have preferred EI to other reanalysis datasets, as it produces robust wave products we can directly rely on without the need of further wave modelling. The EI dataset starts in 1979 and is continuously updated in quasi real time. For our analysis, we have restricted the time interval to the 1992–2016 period (25 years) that, together with the 6-h temporal resolution, allows an adequate description of intra-annual and inter-annual climate cycles (Stopa and Cheung, 2014b). In addition, EI wave

products benefit of the data assimilation of satellite altimeters since August 1991. The assimilation has improved the performance of the model at the expenses of a discontinuity in the 1979-today time series. The macroscopic effect is on significant wave height. Aarnes et al. (2015) have shown that the H_s statistics and trends derived from EI are affected by the introduction of altimeter assimilation, and to a lesser extent by the different satellite updates, the number of operating satellites and the wave data availability. To overcome this issue, our analysis starts in 1992 and pertains to the EI period with the fairest agreement with observations, still covering a 25-year period. The spatial resolution of EI wave products, including wave spectra, is $1.00° \times 1.00°$ (approximately 111 km × 111 km at the equator), provided every 6 h on a global 181 × 360 latitude-longitude regular grid. The EI directional wave spectra $S(\omega, \theta)$ are defined for 30 frequencies (ω) and 24 directions (θ). The quality of EI wave products has been assessed in many studies (see, e.g., Stopa and Cheung, 2014a) that, beside pointing out a better EI performance against observations in the lowest/mid percentiles of wave heights, have qualified it as a robust and reliable dataset, particularly for studies of multi-year signals and climate cycles.

2.2.2. ERA-5

To assess the reliability of the EI-based global analysis we have compared EI results with those obtained from the more recent and higher resolution reanalysis of ECMWF, ERA-5 (henceforth E5). As EI, E5 is a global reanalysis using the same integrated system and two-way coupling the atmospheric and the sea surface wave models. It represents an evolution of EI mostly in being a higher-resolution dataset, both in space and time. We have used hourly wave products with 0.36°x0.36° horizontal resolution (40 km × 40 km at the equator), including directional wave spectra defined for 30 frequencies and 24 directions. E5 also includes 10 lower resolution ensemble members, but they are not taken into account here. The E5 dataset was not available for the extended 1992–2016 period when we did this study, so for our local analysis we have considered 6 years of spectra (2010–2015) in a region (49–51°N, 144–146°W) surrounding the Ocean Weather Station Papa (OWS-P), in the North Pacific Ocean, where a wave measuring buoy is located. Maximum wave heights estimated from those spectra have been then interpolated to get estimates of wave maxima at the buoy location (145°W, 50°N).

2.3. Observational data

The assessment of maximum wave heights from the combination of statistical and numerical (reanalysis) models is done using the observational data provided in the North Pacific Ocean at OWS-P. Two types of wave data are available: single-point (i.e., time) wave measurements recorded at the wave buoy position, and space-time stereo-video data collected from a ship, taken close to the buoy. While single-point data are numerous and available over a long period, we can rely on only two areal datasets at OWS-P, as stereo-video datasets are scarcer with respect to the buoy ones. However, stereo-video datasets are being acquired worldwide and the empirical-theoretical wave maxima agreement has been verified (more are on their way) in several studied (see e.g., Benetazzo et al., 2018, 2017).

The wave buoy is a Datawell directional Waverider. It is managed by the Applied Physics Laboratory of the University of Washington (Seattle, USA) and it represents a long-term observation site in the open ocean as a part of a project studying the effect of surface waves on the ocean mixed layer (Thomson et al., 2013). Deployed firstly in June 2010 on 4255-m deep waters and periodically maintained (the series presents only some short gaps), it continuously collects buoy pitch, roll, and heave data at 1.28 Hz. We have used heave measurements spanning 4.5 years (June 2010-December 2014), during which the buoy has experienced a wide variety of oceanic sea states with significant wave height (H_s) in excess of 3.0 m on average and peaking at 13.7 m. Time

series of heave motion have been employed to obtain empirical estimates of the single-point time extremes $\overline{C}_{max}$, $\overline{H}_{max}$ and $\overline{E}_{max}$ for the observed sea states, assumed of duration $D = 20$ min. Details about the buoy data quality control and the methodology of analysis can be found in Appendix B.

Stereo-video datasets have been acquired in December 2014-January 2015 from the *R/V Thomas G. Thompson*, during a field campaign aimed at the OWS-P buoy maintenance. Several video datasets of sea surface elevation were collected during the cruise (Schwendeman and Thomson, 2017). We have selected two datasets gathered very close to the buoy, collected on January 3rd, 2015, at 20:34UTC and 22:19UTC. The bursts are 30-min long, providing multi-dimensional wave data at 7.5 Hz and framing a sea surface region of about 1000 m², with 0.25 m horizontal resolution. Stereo data encompass sea states with, also crossing, northerly and westerly systems with H_s around 3.60 m. The 3D (2D space + time) sea surface elevation measurements have been used to estimate the empirical values of $\overline{C}_{max}$ and $\overline{H}_{max}$ attained at D-long (time) and XY-wide (space) sea states. We recall that maximum envelope heights have been only estimated in the time domain, as a space-time framework for envelope heights is not developed at present. Details about processing of the stereo data at OWS-P can be found in Schwendeman and Thomson (2017), while the methodology of analysis is described in Appendix B.

3. Assessment of wave extremes at Ocean Weather Station Papa

The first analysis we perform is the assessment of the maximum wave heights prediction using the two sets of observations at OWS-P. At first, the parameters of the statistical models are obtained from the buoy data (heave time series for time extremes, and directional spectra for space-time extremes). Then, we assess the agreement of numerical model estimates, using the two sets of EI and E5 directional spectra.

3.1. Assessment of theoretical predictions

3.1.1. Time extremes from buoy data

Single-point observations and theoretical time extreme model estimates over the 2010–2014 period at the wave buoy are compared in Fig. 1. The values of $\overline{C}_{max}$, $\overline{H}_{max}$ and $\overline{E}_{max}$ show fair agreement between model estimates and observations, with 1.0 correlation coefficients (CC) and Root Mean Square Errors (RMSE) smaller than 0.24 m. Theoretical estimates of $\overline{C}_{max,F}$ and $\overline{E}_{max,J}$ are positively biased with respect to the actual observations (0.11 and 0.07 m, respectively), while those of $\overline{H}_{max,Na}$ are negatively biased (-0.07 m). While $\overline{H}_{max,Na}$ and $\overline{E}_{max,J}$ match (on average) very well the wave height observations (as

indicated by the slope of the best-fit lines, $p = 0.99$ and $p = 1.01$), $\overline{C}_{max,F}$ slightly overestimates the crest height observations (4%, as indicated by p). The linear Rayleigh model (not shown here; CC = 1.00; RMSE = 0.13 m; bias = -0.05 m; $p = 0.98$) fits better the buoy crest height observations with respect to Forristall. This is most likely due to the "linearization effect" experienced by, especially if moored, surface following buoys (see e.g. Casas-Prat and Holthuijsen, 2010), which act as Lagrangian instruments cancelling out the second order non-linearities and producing a general underestimation of the observations with respect to the actual crest heights (Forristall, 2000). In any case, aware of this, we use the Forristall model for time extreme estimates. Indeed, besides showing very good performance at OWS-P as well, it was shown that the contribution of second-order nonlinearities (accounted for by the Forristall model) is determinant in accurately reproducing the time extremes observed using single-point fixed instruments (e.g., wave staffs and radar altimeters from fixed platforms).

3.1.2. Space-time extremes from stereo video data

As far as space-time extremes are concerned, we verify the theoretical estimates versus the stereo-based observations collected on January 3rd, 2015. In Fig. 2, the theoretical mean temporal profiles of STQD (normalized with H_s and zero-crossing mean wave period T_z) are compared to the observed mean profile of the waves with largest C_{max} (see Appendix B for details of data processing). The agreement is good for both the sea states, especially within $\pm 0.5T_m$ from the crest, with nonlinear (STQD2) and linear (STQD1) theoretical profiles in Fig. 2 largely within the experimental confidence interval. As it is expected, STQD2 profiles fit better the observed profiles (higher CC, smaller RMSE, comparable bias), with steeper, higher crest and shallower, flatter troughs than the STQD1 profiles. STQD2 also shows a better agreement with the mean observed crest heights, further confirming the determinant role of second order bound nonlinearities in accurately reproducing maximum wave heights. The non-normalized $\overline{C}_{max}$ for the two sea states are summarized in Table 1, with relative differences in $\overline{C}_{max,STQD2}$ (with respect to observations) at $+1\%$ and -5%, respectively. A third order nonlinear estimate of $\overline{C}_{max}$ accounting for kurtosis effect has been derived (Fedele et al., 2017), but it is not considered here as the contribution of the second order nonlinearities has been shown to be prevailing with respect to the further correction of the third order ones (Fedele et al., 2017). As to $\overline{H}_{max}$, it is worth noting that it is not straightforward to define and detect a single, and worse a maximum, wave height in the 2D space and time. To overcome this issue, we have estimated $\overline{H}_{Cmax}$ rather than $\overline{H}_{max}$, i.e., the largest crest-to-trough excursion in the mean observed temporal profile. The latter has been obtained by averaging the temporal profiles of the waves with
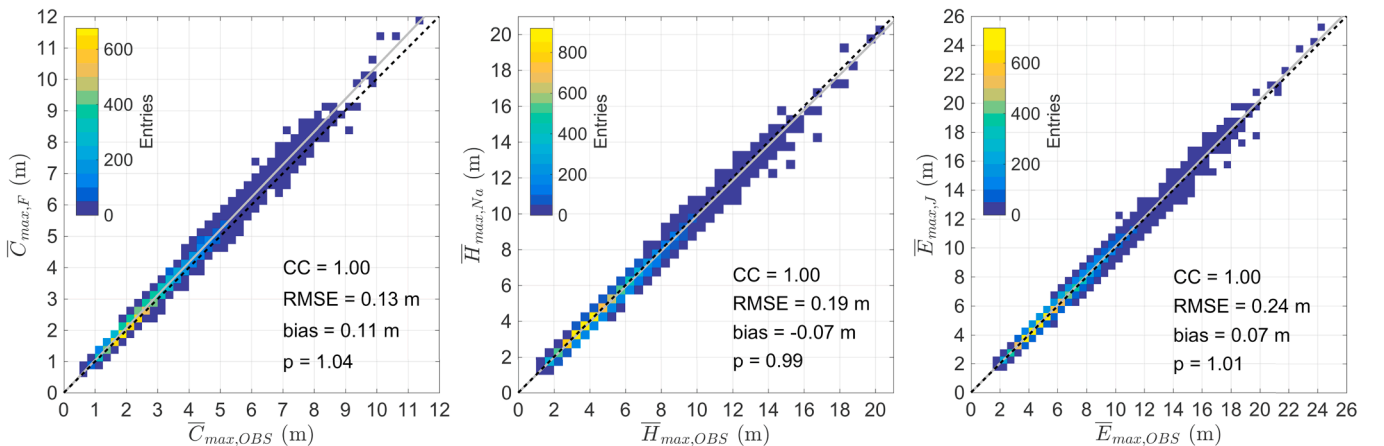

Fig. 1. Comparison of observations (OBS) and theoretically estimated $\overline{C}_{max}$ (left panel, Forristall), $\overline{H}_{max}$ (middle panel, Naess) and $\overline{E}_{max}$ (right panel, Janssen) at a single-point (20-min sea states), OWS-P buoy, North Pacific Ocean, June 2010 – December 2014. The statistics in each panel indicates the correlation coefficient (CC), the centred Root Mean Square Error (RMSE), the model-to-observation bias and the slope (p) of the best-fit line (grey solid line).
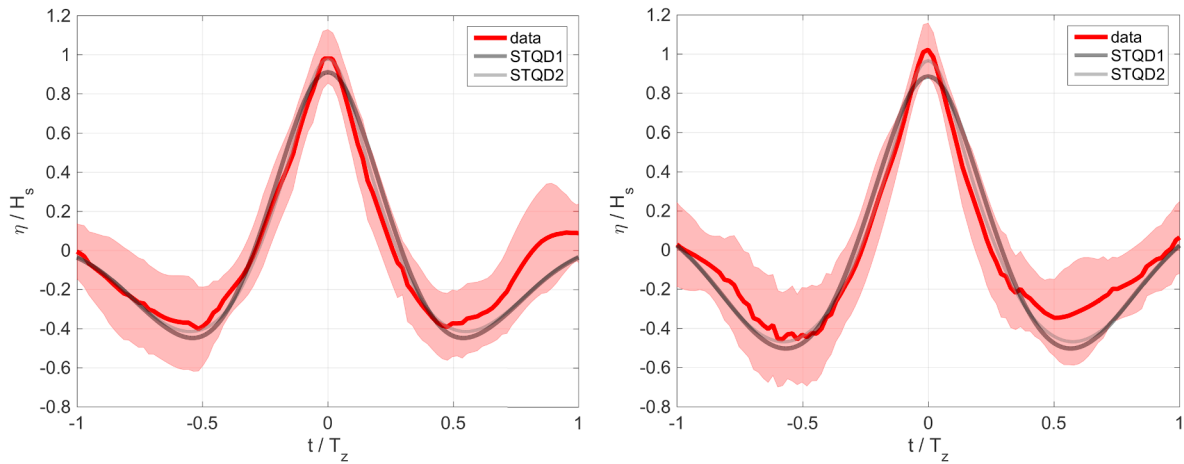
Fig. 2. Comparison of observed (data) and theoretically estimated (linear: STQD1; nonlinear: STQD2) profile η of the waves with the largest crest heights in the stereo datasets close to OWS-P buoy (normalized on H_s and T_z). The observed profile is depicted as the mean (data; red solid line) and standard deviation (red shaded region) of the wave profiles. (left) January, 3rd 2015 at 20:34UTC. STQD2 statistics: CC = 0.98, RMSE = 0.07; bias = 0.02; STQD1 statistics: CC = 0.97, RMSE = 0.09; bias = 0.02. (right) January, 3rd 2015 at 22:19UTC. STQD2 agreement statistics: CC = 0.98, RMSE = 0.07; bias = 0.03; STQD1 agreement statistics: CC = 0.97, RMSE = 0.09; bias = 0.02. (For interpretation of the references to color in this figure legend, the reader is referred to the web version of this article.)

Table 1
Comparison of observed and theoretically estimated (crest height: STQD2; crest-to-trough height: STQD1) $\overline{C}_{max}$ and $\overline{H}_{Cmax}$, in the two stereo datasets close to OWS-P buoy, January 3rd, 2015. $\overline{H}_{Cmax}$ is the mean crest-to-trough height of the waves with maximum crest height. Between parentheses the relative differences of theoretical with respect to observed values.

	January, 3rd 2015 at 20:34UTC		January, 3rd 2015 at 22:19UTC	
	$\overline{C}_{max}$ (m)	$\overline{H}_{Cmax}$ (m)	$\overline{C}_{max}$ (m)	$\overline{H}_{Cmax}$ (m)
Observed	3.56	5.00	3.76	5.46
Theoretical	3.60 (+1%)	4.90 (−2%)	3.58 (−5%)	5.13 (−6%)

largest crest height in the space-time domain. According to Boccotti (2000), $\overline{H}_{Cmax}$ is generally smaller than $\overline{H}_{max}$ (7–10% in typical stormy conditions), unless the spectrum of the sea state is narrow-banded (in such a case, they correspond). In any case, STQD can estimate $\overline{H}_{Cmax}$ and the results in Table 1 show that for the two sea states observed the agreement is within −2% and −6% of observations, respectively. While remarking the importance of the second order nonlinear contribution for the $\overline{C}_{max}$ estimate (for the two sea states close to OWS-P, accounting for the 10% and 9% of the linear estimates, respectively), we point out that the corresponding $\overline{H}_{max}$ estimate is generally smaller (Tayfun and Fedele, 2007). More specifically, in our cases it only accounts for the 2% and 4% of the linear estimate.

3.2. Assessment of ERA-Interim and ERA-5 results

To verify that EI reanalysis spectra can be used to attain a reliable long-term statistics of maximum wave heights, we have assessed the agreement between model estimates based on EI spectra and observations. This analysis, together with the one in the previous Section 3.1, allows us to assess the accuracy of the global long-term estimates, based on EI reanalysis. We are especially interested in quantifying the effect of the spatio-temporal resolution of EI on the estimates of maximum wave heights. To this end, we have also taken into account model estimates based on the higher resolution E5 spectra, comparing them to the EI-based estimates. We use the OWS-P buoy dataset as the main reference for our assessment, since we can rely on a much longer temporal coverage with respect to stereo video experiments. Time extremes from

combined statistical model and reanalysis spectra can be directly compared to buoy observations. To assess the space-time extremes we have to proceed in a different way: granted the observation-model agreement obtained for time extremes with OWS-P buoy dataset and the observation-theoretical model agreement obtained for space-time extremes during the two stereo video experiments, we inter-compare EI to E5 model estimates of space-time extremes over the 2010–2014 period.

3.2.1. Time extremes

The agreement of $\overline{C}_{max}$ from reanalyses and buoy observations is shown in Fig. 3. The scatter plot and statistical parameters point out a very good agreement for both EI (CC = 0.97, RMSE = 0.33 m, bias = 0.05 m, p = 0.96) and E5 (CC = 0.98, RMSE = 0.27 m, bias = 0.02 m, p = 0.98). Actually, this result combines the small overestimate by the statistical model reported above (see Fig. 1, left panel) with a slight spectral misestimate by the reanalyses. The latter manifests itself, for instance, as a slight underestimate of H_s, which however is fairly modelled by EI and E5 (for EI: CC = 0.97, RMSE = 0.39 m, bias = 0.20 m, p = 0.92; for E5: CC = 0.98, RMSE = 0.32 m, bias = 0.19 m, p = 0.93). This holds also for $\overline{C}_{max}$, with E5 performing slightly better than EI, as expected because of the higher spatio-temporal resolution and all the modelling and data analysis progresses in E5.

Similar conclusions can be drawn for $\overline{H}_{max}$ and $\overline{E}_{max}$ (Figs. 4 and 5): the model-observation agreement is very good and comparable for EI- and E5-based estimates. However, the slight underestimate pointed out by the scatter plots and statistical parameters ($\overline{H}_{max}$-EI: CC = 0.97, RMSE = 0.62 m, bias = −0.32 m, p = 0.92; $\overline{H}_{max}$-E5: CC = 0.98, RMSE = 0.52 m, bias = −0.32 m, p = 0.93; $\overline{E}_{max}$-EI: CC = 0.97, RMSE = 0.67 m, bias = −0.34 m, p = 0.93; $\overline{E}_{max}$-E5: CC = 0.98, RMSE = 0.56 m, bias = 0.87 m, p = 0.94) can be mostly ascribed to the reanalysis performance, as $\overline{H}_{max}$ and $\overline{E}_{max}$ theoretical estimates have been shown to be excellent (see Fig. 1, middle and right panels). Again, E5 performs slightly better than EI, but statistics are very similar, with the only exception for the $\overline{E}_{max}$ model-to-observation bias that is positive (otherwise always negative) and larger in case E5 is used.

We have also compared the 50th (median) and 99th percentiles, to verify the model-observation agreement in typical and extreme conditions, respectively. The results are summarized in Table 2, where, beside reanalyses, the theoretical estimates (from the observed spectra)
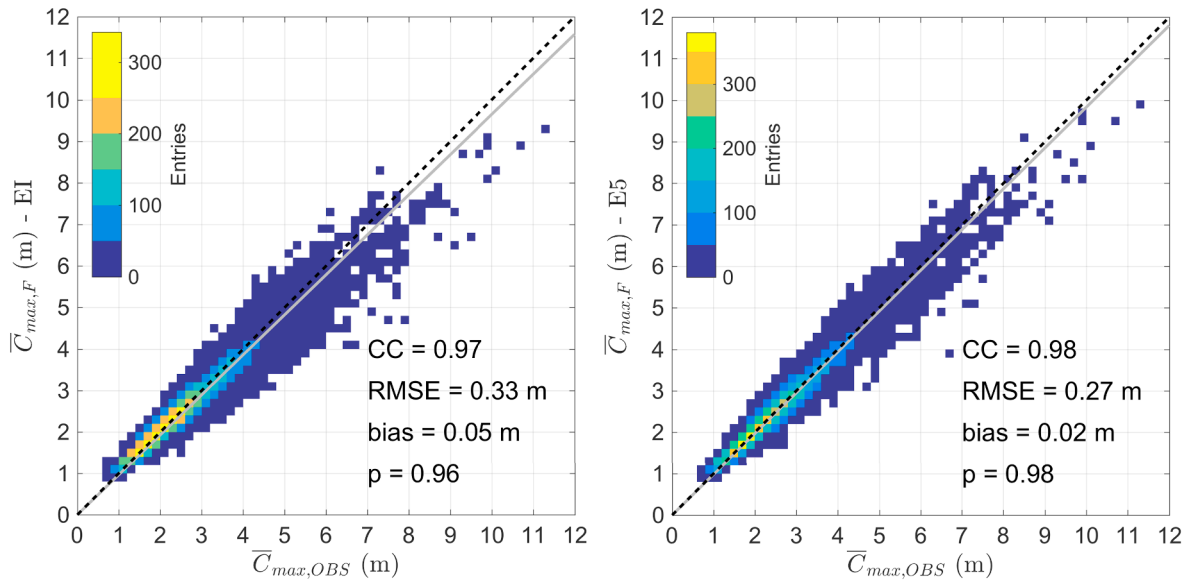
Fig. 3. Comparison of observations (OBS) and theoretically estimated $\overline{C}_{max}$ from EI (left panel) and E5 (right panel) spectra at the OWS-P buoy, North Pacific Ocean, June 2010 – December 2014. The statistics in each panel indicates the correlation coefficient (CC), the centred Root Mean Square Error (RMSE), the model-to-observation bias and the slope (p) of the best-fit line (grey solid line).

are compared to the actually observed values. It is worth noting the excellent theoretical agreement on $\overline{H}_{max}$ (-1.5% and -1.3% relative differences with 50th and 99th percentiles of observations, respectively) and $\overline{E}_{max}$ (1.1% and 1.7%), as well as the slight overestimate of $\overline{C}_{max}$ (3.9% and 4.7%). We recall however that buoy crest height observations may be underestimated because of the already cited buoy dynamics and linearization effect (see Section 3.1.1). As to EI and E5, we point out a comparable and very good performance for the 50th percentiles of all the heights and a significantly better performance of E5 compared to EI for the 99th percentile, the latter underestimated of 7.2% for $\overline{C}_{max}$, 12.2% for $\overline{H}_{max}$ and 9.4% for $\overline{E}_{max}$. This is consistent with the conclusions of Stopa and Cheung (2014a), who pointed out that EI performs better in ordinary (i.e., the lowest percentiles) than extreme

(i.e., the highest percentiles) conditions, with respect to other re-analysis datasets.

3.2.2. Space-time extremes

The agreement between EI and E5 estimates of space-time extremes can be assessed with scatter plots and statistics in Fig. 6. The slope of the best fit line (0.97 for $\overline{C}_{max}$ and 0.98 for $\overline{H}_{max}$) and the negative bias (-0.10 for $\overline{C}_{max}$ and -0.08 for $\overline{H}_{max}$) point out a general small underestimate of EI with respect to E5, for both $\overline{C}_{max}$ and $\overline{H}_{max}$, supporting the results already shown for time extremes. However, besides this, the agreement is good.

We can conclude that, as expected, E5 estimates of $\overline{C}_{max}$, $\overline{H}_{max}$ and $\overline{E}_{max}$ are in a better agreement with observations at OWS-P with respect
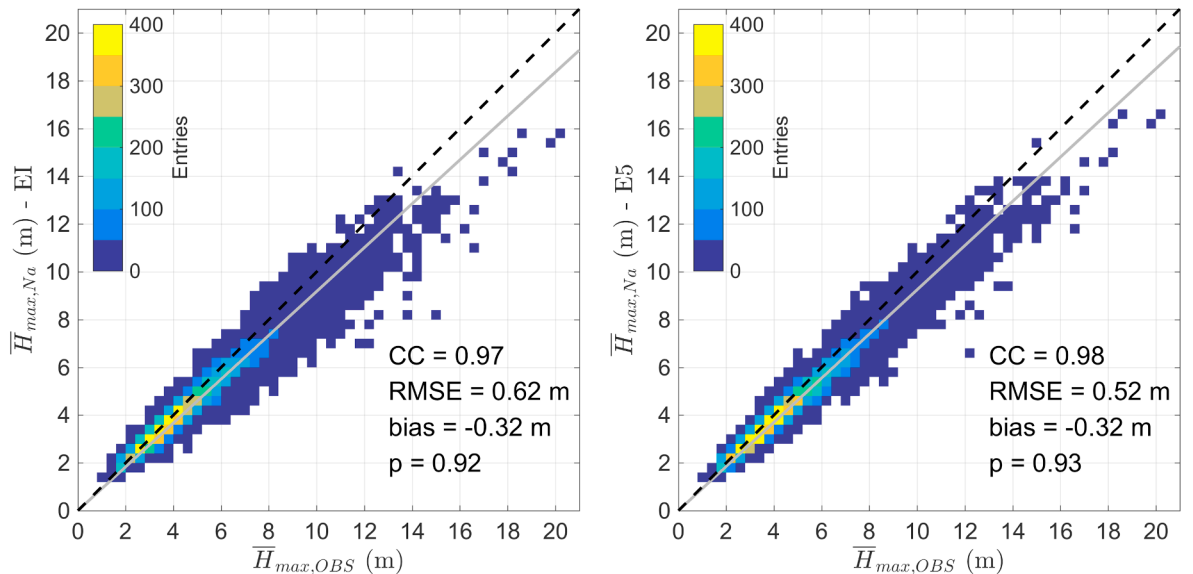
Fig. 4. Comparison of observations (OBS) and theoretically estimated $\overline{H}_{max}$ from EI (left panel) and E5 (right panel) spectra at the OWS-P buoy, North Pacific Ocean, June 2010 – December 2014. The statistics in each panel indicates the correlation coefficient (CC), the centred Root Mean Square Error (RMSE), the model-to-observation bias and the slope of the best-fit line (p).
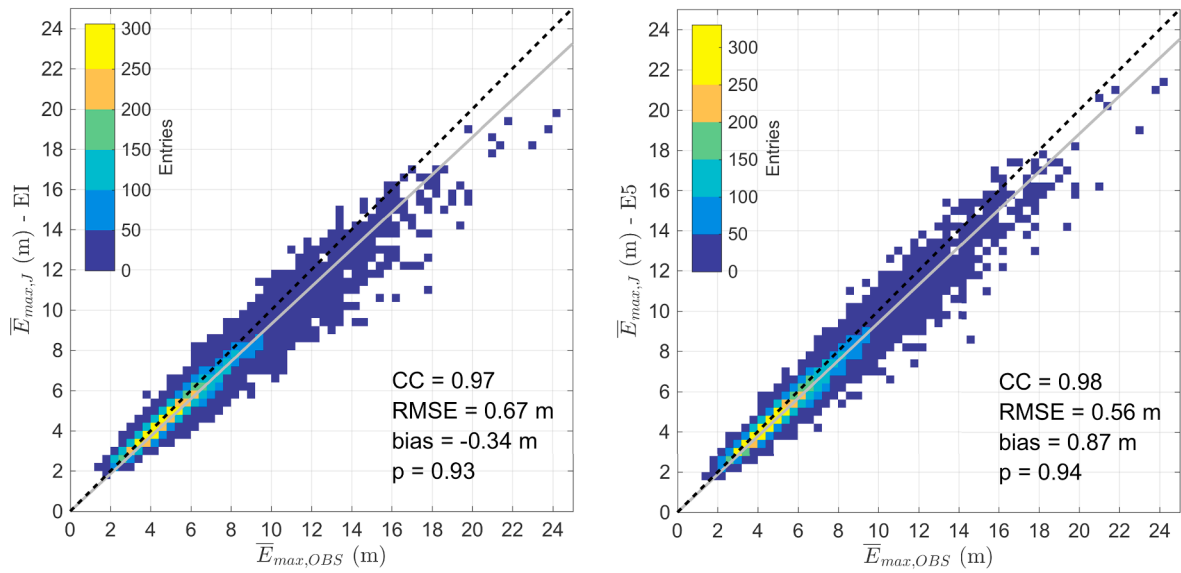
Fig. 5. Comparison of observations (OBS) and theoretically estimated $\overline{E}_{max}$ from EI (left panel) and E5 (right panel) spectra at the OWS-P buoy, North Pacific Ocean, June 2010 – December 2014. The statistics in each panel indicates the correlation coefficient (CC), the centred Root Mean Square Error (RMSE), the model-to-observation bias and the slope (*p*) of the best-fit line (grey solid line).

Table 2
50th and 99th percentiles of the single-point (20-min) $\overline{C}_{max}$, $\overline{H}_{max}$ and $\overline{E}_{max}$ at OWS-P (North Pacific Ocean; June 2010 – December 2014), as estimated from observations (OBS), the statistical model with observed spectrum (TH) and the statistical model with reanalysis spectra (EI: ERA Interim; E5: ERA 5). Between parentheses the relative differences with respect to observed values.

$\overline{C}_{max}$ (m)	OBS	TH	EI	E5
50th percentile	2.57	2.68 (3.9%)	2.55 (-0.8%)	2.58 (0.1%)
99th percentile	6.81	7.14 (4.7%)	6.32 (-7.2%)	6.56 (-3.8%)

$\overline{H}_{max}$ (m)	OBS	TH	EI	E5
50th percentile	4.59	4.52 (-1.5%)	4.35 (-5.4%)	4.33 (-5.6%)
99th percentile	12.29	12.13 (-1.3%)	10.79 (-12.2%)	11.11 (-9.6%)

$\overline{E}_{max}$ (m)	OBS	TH	EI	E5
50th percentile	5.68	5.74 (1.1%)	5.42 (-4.6%)	5.41 (-4.8%)
99th percentile	14.92	15.18 (1.7%)	13.52 (-9.4%)	14.06 (-5.8%)

to EI. This is highlighted mostly by smaller RMSE and *p* closer to 1. However, the difference between the E5 and EI performances is small, especially in the typical conditions (i.e., 50th percentiles, where EI does better than E5), in a way that it allows to use EI for the global assessment of wave extremes, aware of possible underestimates at the highest percentiles (reasonably within 12%). In addition, the 25-year coverage of EI is a fundamental requirement for a long-term, i.e., climate, analysis.

4. Global long-term statistics of maximum wave heights

We present in this section the results of the global analysis of maximum wave heights based on the 25-year long EI dataset. To determine the long-term distribution of maximal waves and its features, we combine the short-term (i.e., sea state scale) and long-term statistics of $\overline{C}_{max}$, $\overline{H}_{max}$ and $\overline{E}_{max}$. Firstly, following an *initial-distribution* approach (Holthuijsen, 2007), we take into account all the available values of $\overline{C}_{max}$, $\overline{H}_{max}$ and $\overline{E}_{max}$ at each location, and we derive the typical and extreme conditions, here respectively represented by the 50th (i.e., the median) and 99th percentiles (i.e., the value exceeded 1% of the times; in agreement with Young et al., 2011). These estimates can find

application, for instance, in ship routing. Secondly, following an *annual-maximum* approach, we derive the $\overline{C}_{max}$, $\overline{H}_{max}$ and $\overline{E}_{max}$ with 50-year return period from the 25-year dataset, this long-term statistical feature being widely used for structural design purposes. We have preferred this approach to, for instance, the Peak-Over-Threshold (POT) approach, as we want to avoid dependence of the results upon the chosen threshold. Beside this, applying POT on a global scale may be computationally quite demanding. However, both the approaches are theoretically supported and allow independent and identically distributed sample to be used for the extreme value analysis. To our end, we fit a Gumbel (1958) distribution to the 25 annual maxima at each location of the global seas. The locations where the sample size is smaller than 25 continuous years (e.g., where there is seasonal ice coverage, hence temporary lack of wave model spectra), although not excluded from the computation, are marked with white dots, in order to indicate where estimates may be not homogeneous.

In these analyses, $\overline{C}_{max}$, $\overline{H}_{max}$ and $\overline{E}_{max}$ are thus treated as random variables and a stationary wave climate is assumed. The latter assumption, although not verified, has been accepted, as there is not a consensus on the existence of clear trends in the global past-present wave climate. Indeed, based on the EI dataset, Aarnes et al. (2015) have found regions with slightly negative or no trends (e.g., North Atlantic and North Pacific oceans), as well as regions with positive trends of H_s (e.g., South Pacific). On the contrary, Cox and Swail (2001) have found positive trends of H_s in the North-East Atlantic and negative trends in the South Pacific, using a 40-year global wave simulation. Relying on altimeter data, Young et al. (2012) have found no clear trend for the 100-year return period H_s. In addition, the statistical significance and the uncertainties connected to such trend assessments and quantifications should be taken into account. Hence, we have assumed a stationary wave climate, aware, however, that our results hold strictly in this condition.
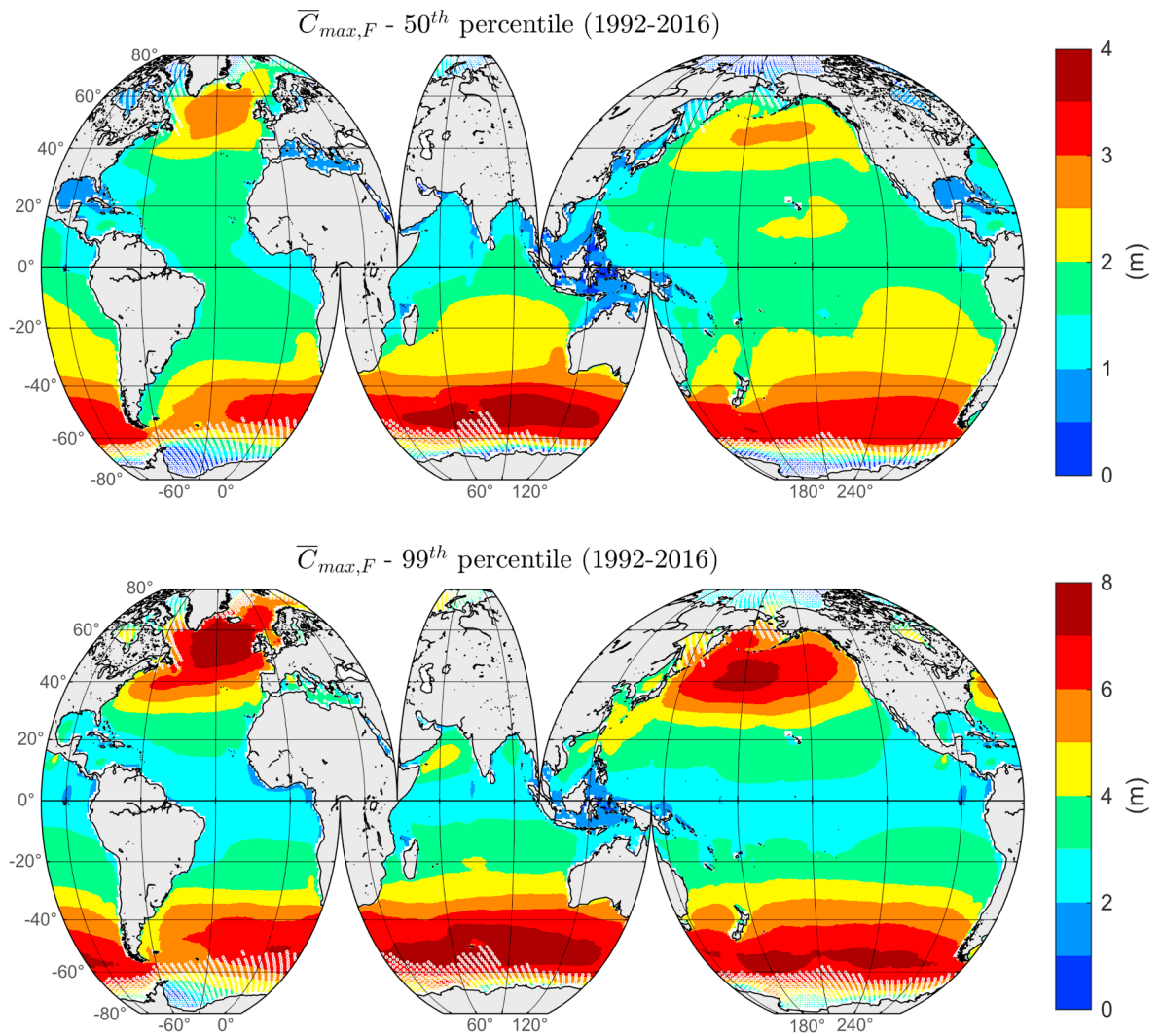
The Mollweide geographical projection is used to show the results, thus focusing the attention on the three major oceans: Atlantic on the left, Indian in the middle, and Pacific on the right.

4.1. Crest heights

We present the global assessment of maximum crest heights, first following the time extreme approach and then extending the analysis to the space-time extremes. Fig. 7 shows the 50th (top panel) and 99th
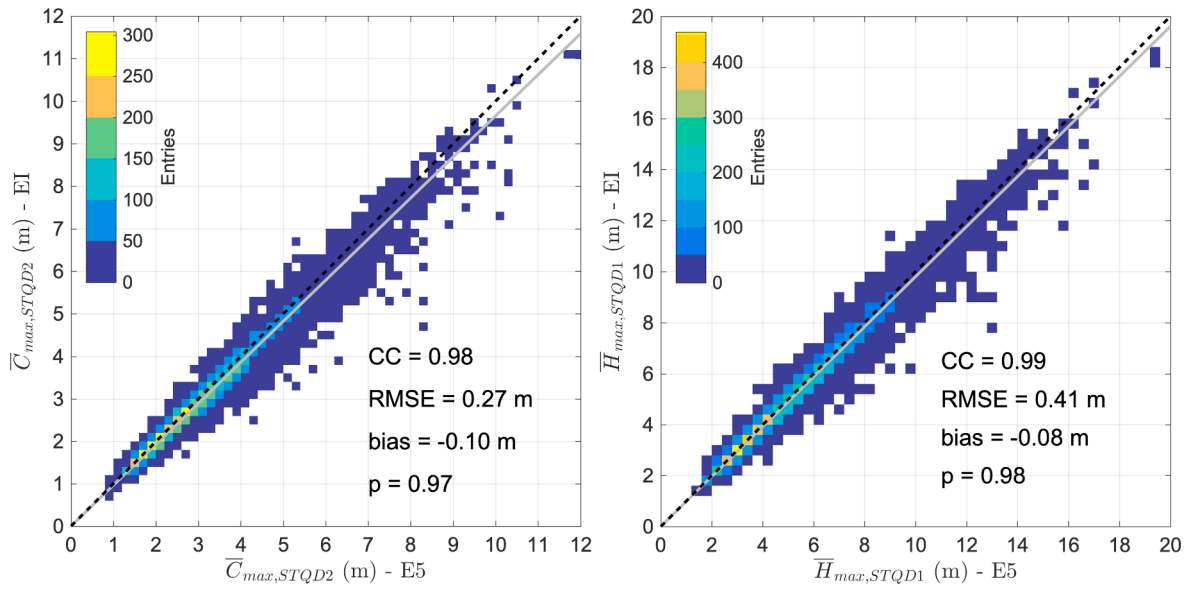
Fig. 6. Comparison of $\overline{C}_{max,STQD2}$ (left) and $\overline{H}_{max,STQD1}$ (right) from EI and E5 spectra at the OWS-P buoy, North Pacific Ocean, June 2010 – December 2014. The statistics in each panel indicates the correlation coefficient (CC), the centred Root Mean Square Error (RMSE), the model-to-observation bias and the slope (*p*) of the best-fit line (grey solid line).

$$\overline{C}_{max,F} - 50^{th} \text{ percentile } (1992\text{-}2016)$$

$$\overline{C}_{max,F} - 99^{th} \text{ percentile } (1992\text{-}2016)$$

Fig. 7. Long-term global assessment of the single-point $\overline{C}_{max,F}$ (20 min) from EI. The white dots close to the poles indicate locations where there is lack of wave spectra, e.g., due to seasonal ice coverage.

(bottom panel) percentiles of the 20-min $\overline{C}_{max,F}$ over the world oceans. The first and most impressive piece of information, in both the panels, is the zonal arrangement of the $\overline{C}_{max,F}$ values, with the highest values spread over the extra-tropical latitudes (only interrupted by continents in the boreal hemisphere), and the lowest ones in the intra-tropical and equatorial latitudes. The former are indeed dominated by wind waves forced by westerlies, while the latter are mainly dominated by the swells propagating from higher latitudes and the weak trade-wind generated waves (Young, 1999). What particularly draws the attention is the uninterrupted circular path of high $\overline{C}_{max,F}$ over the southern parts of the three oceans (between 30°S and 60°S). Here, specifically in the southern part of the Indian Ocean where winds are stronger than in the rest of the zonal belt (Young, 1999), the maximum global 50th and 99th percentiles of $\overline{C}_{max,F}$ (4 and 8 m, respectively) are attained. The largest values, particularly in the southern part of the Indian Ocean, can be associated to the larger values of the steepness (μ, see definition in Appendix A) that characterize that stormy zone, as we will show in Section 5. The only exception at these latitudes is South Atlantic, towards the Argentinian coast, having smaller values due to the local reduced fetch lengths of the westerlies. In the boreal hemisphere, the highest values of $\overline{C}_{max,F}$ are attained in two vast regions of the North

Atlantic and North Pacific oceans, respectively. In the Atlantic, the area with the largest 50th percentile of $\overline{C}_{max,F}$, up to 3 m, is bounded to the west by Labrador, to the north by Greenland and Iceland, and to the east by Ireland and Great Britain. In the same area 8 m can be attained (99th percentile of $\overline{C}_{max,F}$). In the Pacific, the highest $\overline{C}_{max,F}$, both 50th and 99th percentiles (up to 3 and 8 m, respectively) are localized in the north, between the Asian and American continents, south of the Bering Sea.

There are details deserving attention also in the intra-tropical region. For instance, local areas where the 99th percentile of $\overline{C}_{max,F}$ is much larger than in the neighbourhood, causing significant spatial gradients. One of this spots is in the central Pacific Ocean, off the west coast of Mexico, where there is a clearly visible narrow jet of 4–5 m entering a vast region with lower (here, 2–3 m) $\overline{C}_{max,F}$. Another example is in the Indian Ocean, in the Arabian Sea, where the winter and summer Monsoons can produce rough conditions for an otherwise rather calm region. These cases contribute to qualifying the intra-tropical latitudes of the three oceans as typically mild regions (maximum $\overline{C}_{max,F}$ of 2.5 m, in the central Pacific), compared to the northern and southern parts, but with locally severe conditions.

We now extend to the 3D space-time domain the single-point 20-
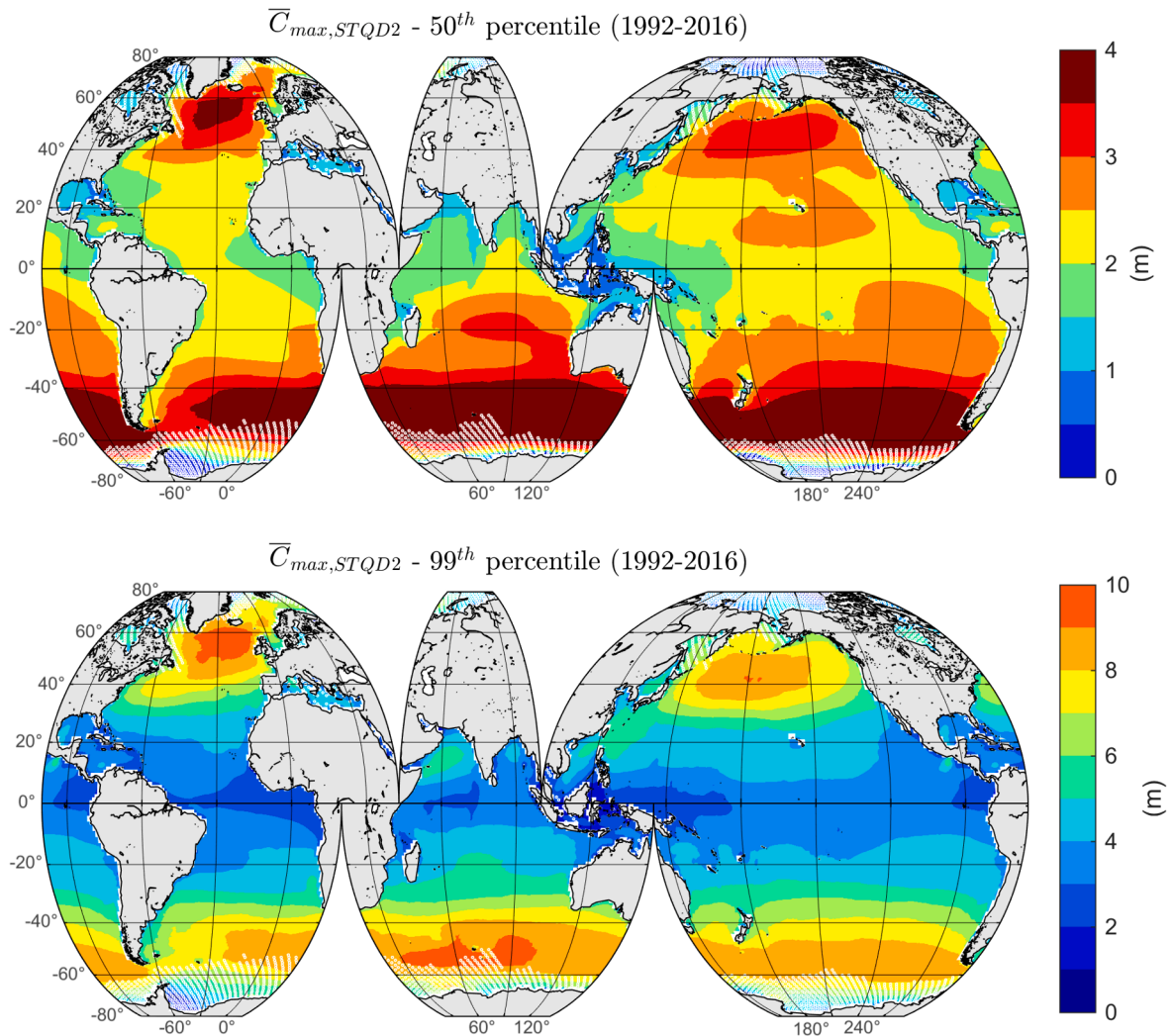
Fig. 8. Long-term global assessment of the space-time $\overline{C}_{max,STQD2}$ (20 min, 100 × 100 m^2) from EI. The white dots close to the poles indicate locations where there is lack of wave spectra, e.g., due to seasonal ice coverage.

min estimate of $\overline{C}_{max}$, thus including the effect of the 3D geometry and short-crestedness of ocean waves on the wave statistics. As already specified, we have selected a square sea surface region of area $100 \times 100\,\text{m}^2$, which can be considered "typical" of an offshore rig size. Fig. 8 shows the maps of 50th and 99th percentiles of $\overline{C}_{max,STQD2}$. Beside observing that spatial patterns are similar to those of $\overline{C}_{max,F}$ (Fig. 7), it is worth noting that values are globally larger, with vast areas reaching the maximum (4 m for 50th and 10 m for 99th percentile). On average, the 50th percentile space-time extremes are 32% larger than the time extremes, and the 99th percentile space-time extremes are 27% larger, with largest space-time to time ratios at low latitudes (not shown here). However, the most severe zones are the high latitudes, particularly beyond the 40°. There, the 50th percentile $\overline{C}_{max,STQD2}$ widely reach 3 m in the boreal hemisphere (4 m in the North Atlantic Ocean) and 4 m in the austral hemisphere, with only limited local exceptions. The 99th percentile reaches 7 m almost everywhere in both the hemispheres, over the 40° (even over the 30° in the North Pacific). The maximum height of 10 m is attained in the North Atlantic, North Pacific and Indian Ocean.

The long-term features of maximal wave crest heights are here characterized in terms of the 50-year return period $\overline{C}_{max,F}$ and $\overline{C}_{max,STDQ2}$, plotted in Fig. 9. Although by and large the spatial patterns resemble those of the 99th percentiles of both parameters, there are a couple of peculiarities that deserve attention. First, the fields are less smooth than the 99th percentiles, with stronger local gradients, especially in the south-western (north of New Zealand) and north-eastern parts of the Pacific Ocean, and in the southern part of the Indian Ocean (east of Madagascar). Second, and in contrast with 99th percentile maps, $\overline{C}_{max,F}$ and $\overline{C}_{max,STDQ2}$ are larger in the northern hemisphere than in the southern one, or at least, the areas reaching the maximal values, i.e., 14 m for $\overline{C}_{max,F}$ and 16 m for $\overline{C}_{max,STDQ2}$, are wider in the North Atlantic and North Pacific oceans, which are shown to be the most severe seas.

4.2. Crest-to-trough heights

We now present the long-term global estimates of maximum crest-to-trough heights, starting from the time extreme estimates and then
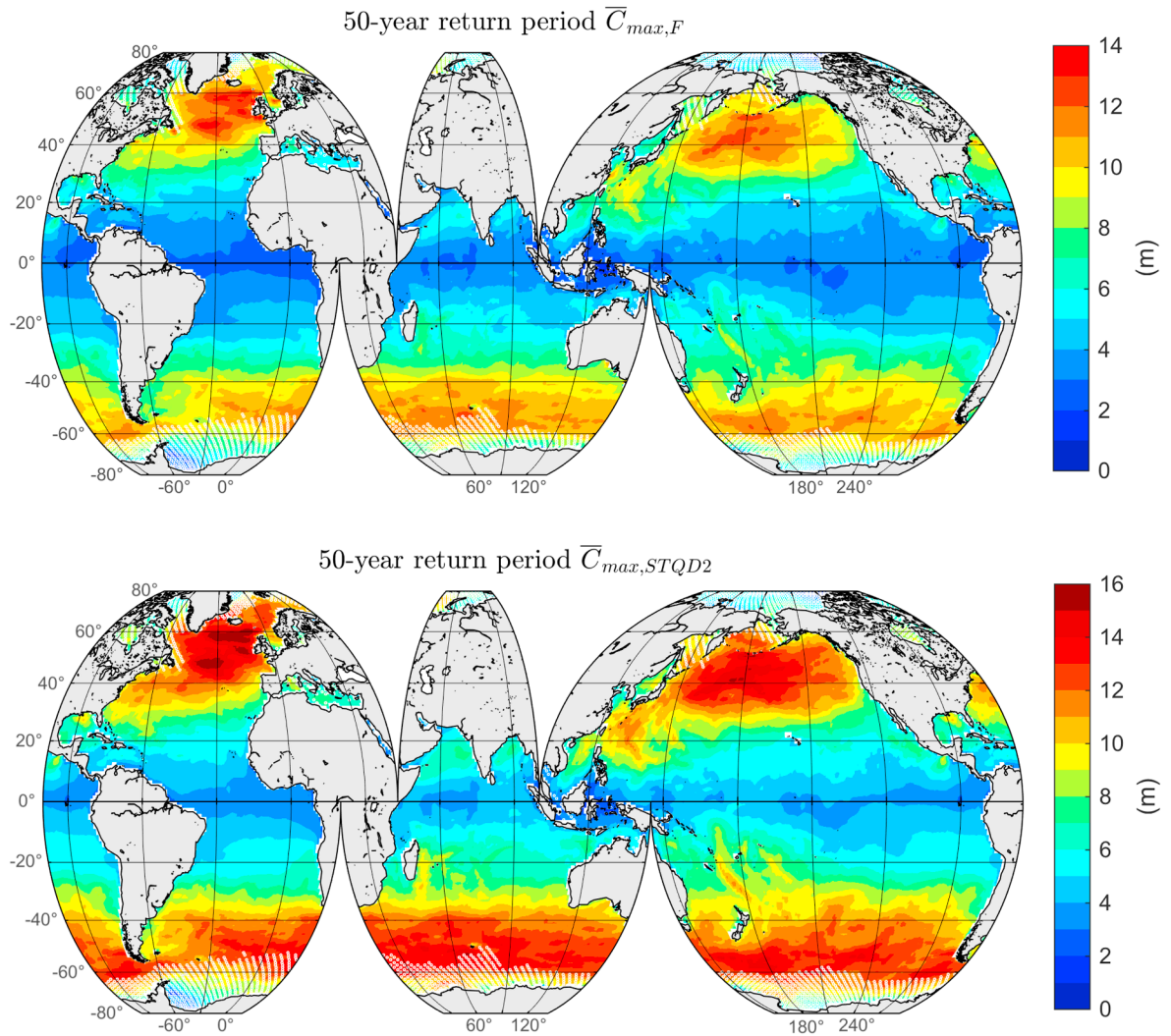
Fig. 9. Long-term global assessment of the single-point (20 min) $\overline{C}_{max,F}$ (top) and the space-time (20 min, $100 \times 100\,\text{m}^2$) $\overline{C}_{max,STQD2}$ (bottom) with return period R = 50 years from EI. The white dots close to the poles indicate locations where there is lack of wave spectra, e.g., due to seasonal ice coverage.

moving to the space-time extremes. The values of the 20-min $\overline{H}_{max,Na}$ over the world oceans are shown in Fig. 10 (50th percentile in the top panel, 99th percentile in the bottom). As expected, the spatial patterns of $\overline{H}_{max,Na}$ are rather similar to those outlined for $\overline{C}_{max,F}$, i.e., the zonal arrangement with highest values in the southern oceans and in the North Atlantic and North Pacific oceans, and lowest values in-between and around the tropics. The reason is that the spatial arrangement of maximum crest-to-trough heights, as well as that of crest heights, reflects the spatial arrangement of H_s, which provides the total energy of the sea states (see Section 5). The largest values of $\overline{H}_{max,Na}$ (50th percentile up to 6 m, 99th percentile up to 14 m) occur in the southern oceans, but North Atlantic and North Pacific oceans can reach comparable values of the 99th percentile $\overline{H}_{max,Na}$. Note that, while North Atlantic and North Pacific have comparable 50th percentiles of $\overline{C}_{max,F}$, the 50th percentile of $\overline{H}_{max,Na}$ is larger in the North Atlantic than in the Pacific. This difference can be explained in the light of the larger 50th

percentiles of H_s and ψ^* (minimum of the autocovariance function, defined in Appendix A) observed in the North Atlantic (see Section 5). Larger ψ^* means narrower frequency spectra, as opposed to the wider North Pacific spectra, often a mixture of local wind sea and different swells coming from the south.

Moving to the space-time extremes and evaluating $\overline{H}_{max,STQD1}$ on a $100 \times 100\,m^2$ area (over 20 min), we can do similar considerations done for $\overline{H}_{max,Na}$ for the maps of 50th and 99th percentiles of $\overline{H}_{max,STQD1}$, which are shown in Fig. 11. The largest values (8 m for 50th, 16 m for 99th percentile) are again found over the mid latitude zonal regions. On average, 50th percentile $\overline{H}_{max,STQD1}$ are 27% larger than corresponding $\overline{H}_{max,Na}$ and 99th percentile $\overline{H}_{max,STQD1}$ are 19% larger than corresponding $\overline{H}_{max,Na}$. Thus, the underestimate of single-point $\overline{H}_{max}$ with respect to areal ones is the largest the most typical conditions are, which we have shown is also true for $\overline{C}_{max}$. This is confirmed by the comparison of extreme (50-year return period) values over an area and
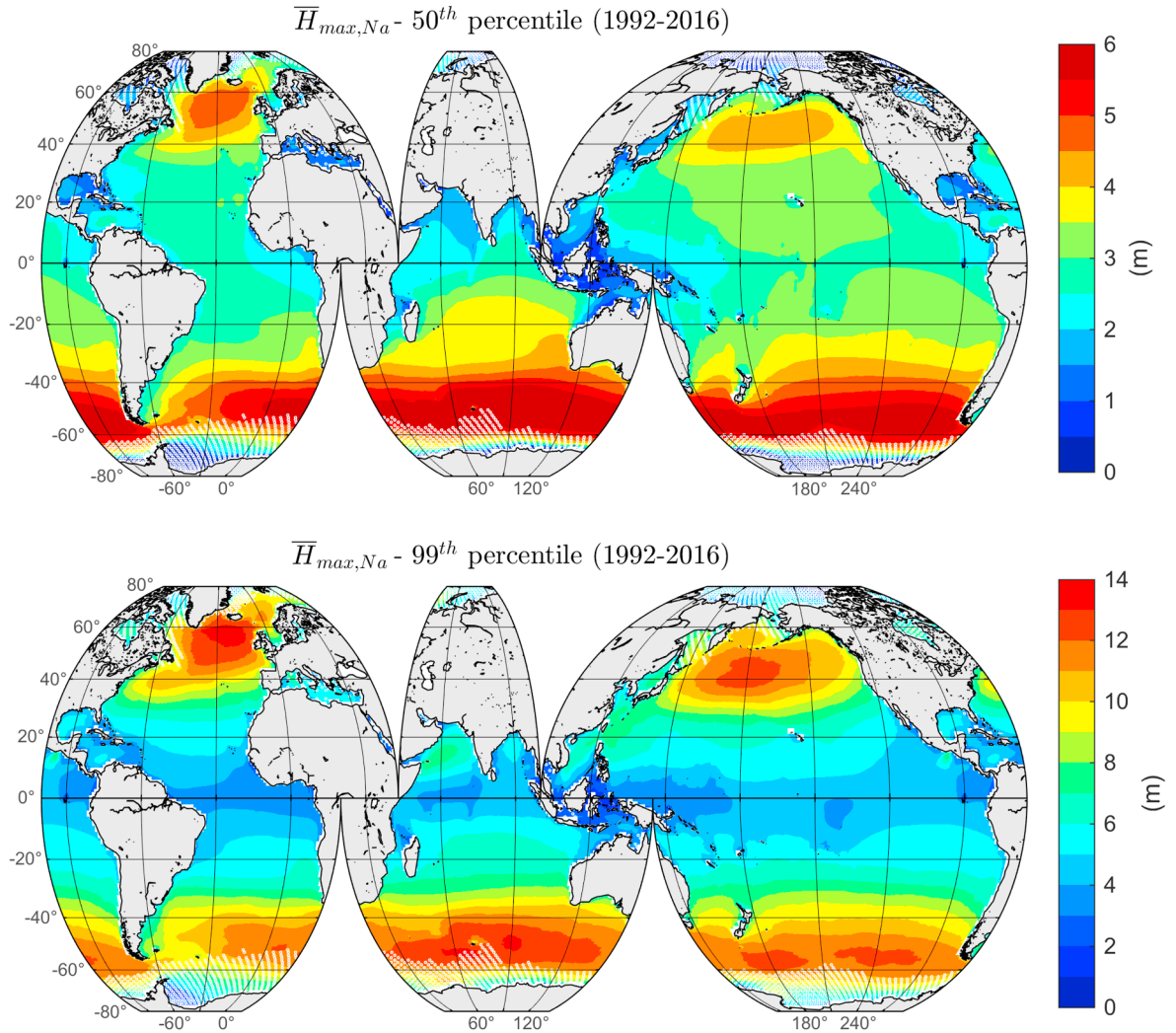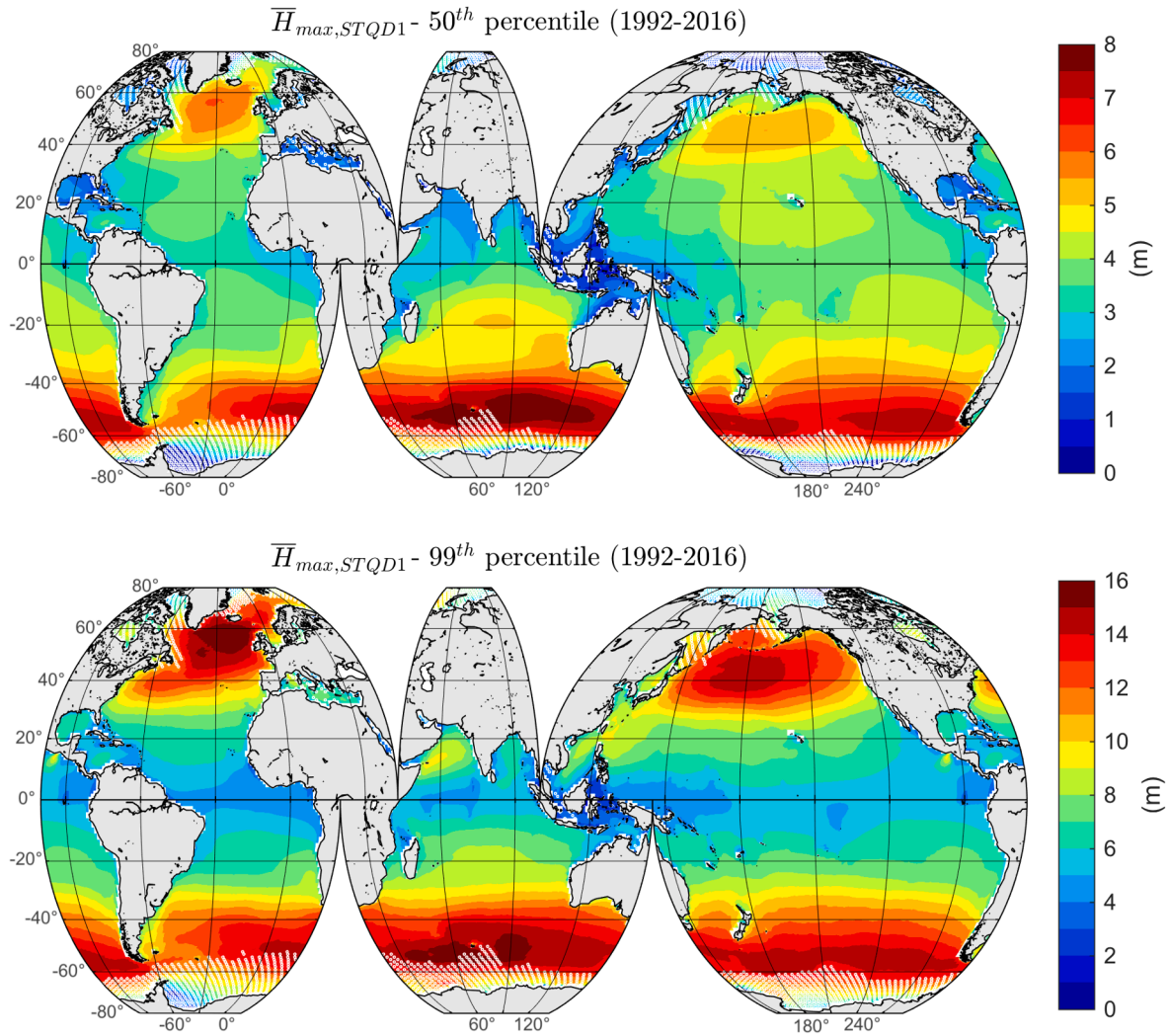

Fig. 10. Long-term global assessment of the single-point $\overline{H}_{max,Na}$ (20 min) from EI. The white dots close to the poles indicate locations where there is lack of wave spectra, e.g., due to seasonal ice coverage.

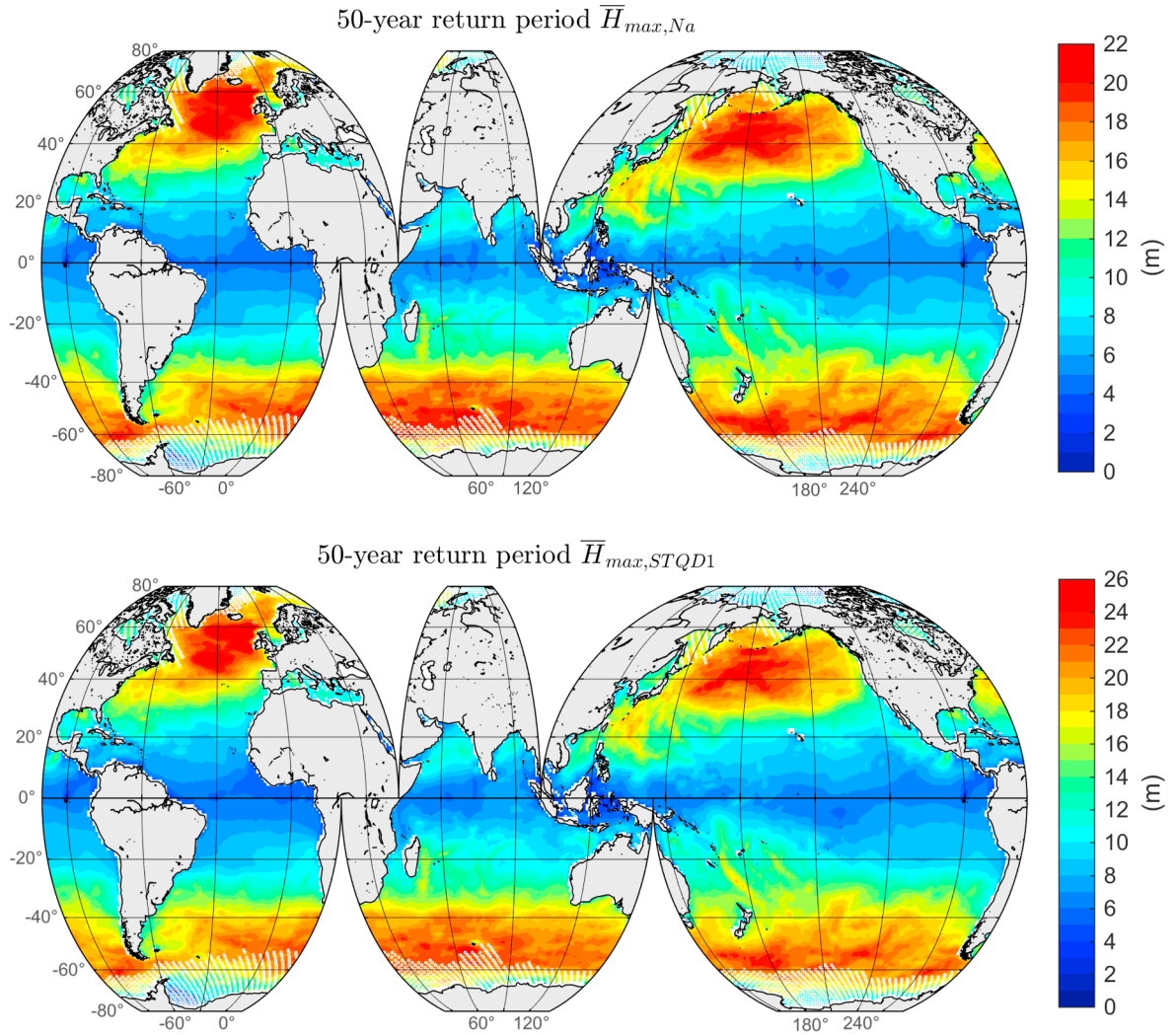**Fig. 11.** Long-term global assessment of the space-time $\overline{H}_{max,STQD1}$ (20 min, 100×100 m^2) from EI. The white dots close to the poles indicate locations where there is lack of wave spectra, e.g., due to seasonal ice coverage.

at a single-point (Fig. 9 for $\overline{C}_{max}$, Fig. 12 for H_{max}). Indeed, 50-year $\overline{C}_{max}$ and $\overline{H}_{max}$ are 23% and 20% larger if assessed over 100×100 m^2, i.e., again higher than single-point equivalents, but to a smaller extent with respect to the 50th percentiles and to a smaller or almost equal extent with respect to the 99th percentiles. Extreme values of $\overline{H}_{max,Na}$ and $\overline{H}_{max,STQD1}$ can reach 22 m and 26 m, respectively, in the North Atlantic and North Pacific oceans, which are confirmed to be the most severe seas.

4.3. Envelope heights

We now present the global long-term estimates of maximum envelope height, which has been evaluated over the time domain only, i.e., at a single-point. The 50th and 99th percentiles of the 20-min $\overline{E}_{max,J}$

over the world oceans are shown in Fig. 13. The spatial arrangement resembles, also in this case, those of the other maximum wave heights presented above and that of H_s (see Section 5). However, we can quantitatively assess the typical (i.e., 50th percentile) and extreme (i.e., 99th percentile) envelope height conditions that can respectively reach 8 m (in the southern part of the Indian Ocean) and 16 m (in the southern part of the Indian and in the northern part of the Atlantic and Pacific oceans). Comparing the estimates of $\overline{E}_{max,J}$ (Fig. 13) and $\overline{C}_{max,F}$ (Fig. 9) it is interesting to note that the envelope-to-crest height ratio is on average about 2 (not shown here). Provided the definition of the envelope height (twice the maximum amplitude of the envelope, i.e., very close to maximum crest height), this result would suggest that the third order nonlinear contribution to the crest height is small compared to the second order one. Comparing the estimates of $\overline{E}_{max,J}$ (Fig. 13) and

50-year return period $\overline{H}_{max,Na}$

50-year return period $\overline{H}_{max,STQD1}$

Fig. 12. Long-term global assessment of the single-point (20 min) $\overline{H}_{max,Na}$ (top) and of the space-time (20 min, 100 × 100 m²) $\overline{H}_{max,STQD1}$ (bottom) with return period R = 50 years from EI. The white dots close to the poles indicate locations where there is lack of wave spectra, e.g., due to seasonal ice coverage.

$\overline{H}_{max,Na}$ (Fig. 10), it can be shown (not here) that maximum envelope heights are on average 1.25 times larger than maximum crest-to-trough heights, this difference being imputable partly to the different definition, partly to different model adopted (nonlinear for $\overline{E}_{max}$, linear for $\overline{H}_{max}$). We point out that the largest values of kurtosis (definition in Appendix A), mainly located over the western portions of the Atlantic and Pacific Oceans (see Section 5), contribute in producing there the largest values of $\overline{E}_{max,J}$ together with the largest values of H_s. The 50-year return period $\overline{E}_{max,J}$ are shown in Fig. 14, with maximal values, i.e., 28 m, attained again over portions of the North Atlantic and North Pacific oceans.

5. Discussion

In Section 4, we have presented an assessment of time and space-time maximum wave heights over the world oceans. Doing so, we have provided a quantitative characterization of global maximum expected crest, crest-to-trough and envelope heights, also following different approaches, which however share common features and spatial

patterns. In particular, the latter ones largely reflect the spatial distribution of H_s, which is shown in the top panels of Fig. 15 (left: 50th percentile, right: 99th percentile). However, although H_s is a proxy of the wave energy and provides the principal scale parameter for maxima, the normalized heights $\overline{C}_{max}H_s^{-1}$, $\overline{H}_{max}H_s^{-1}$ and $\overline{E}_{max}H_s^{-1}$ depends largely upon the shape of the directional spectrum (see Appendix A), the nonlinearity of the sea state (μ, the integral steepness, and κ, the kurtosis) and its irregularity (ψ^*, the minimum of the autocovariance function). All those parameters, as well as H_s, vary over the world oceans with spatial patterns related to the zonal and local wave climate. Here, we show the global assessment of μ (Fig. 15, top-middle panels), κ (Fig. 15, bottom-middle panels) and ψ^* (Fig. 15, bottom panels). We note that the steepest sea states are located in the storm belts, between 30°N (S) and 60°N (S), particularly in the South Atlantic and Indian oceans, and over the western part of the North Atlantic and North Pacific oceans, the latter dominated by the younger sea states generated by the westerlies. North Atlantic and North Pacific oceans are the regions where also the kurtosis κ, another parameter accounting for the nonlinearity of the sea states as μ, is larger. The storm belt regions are
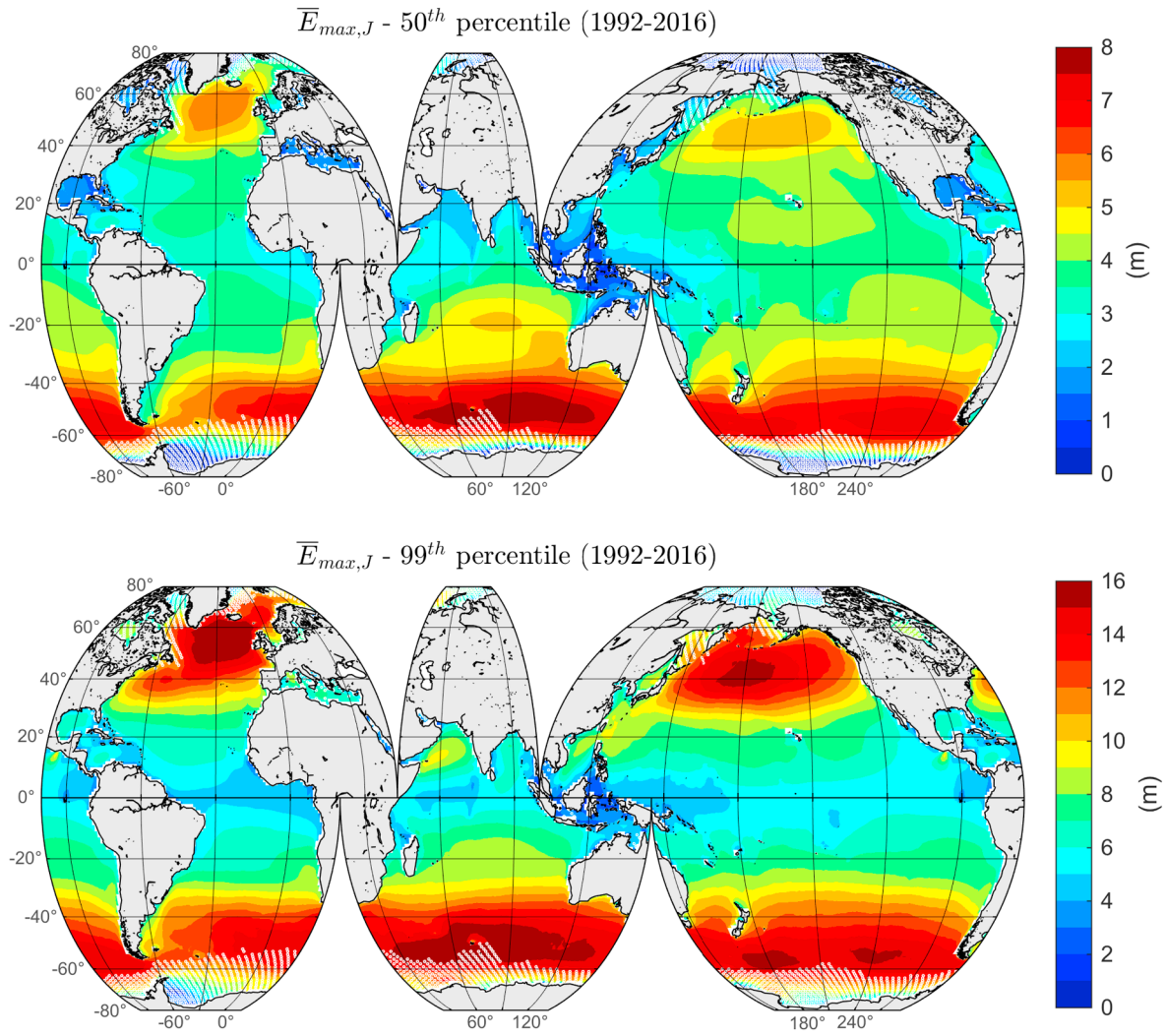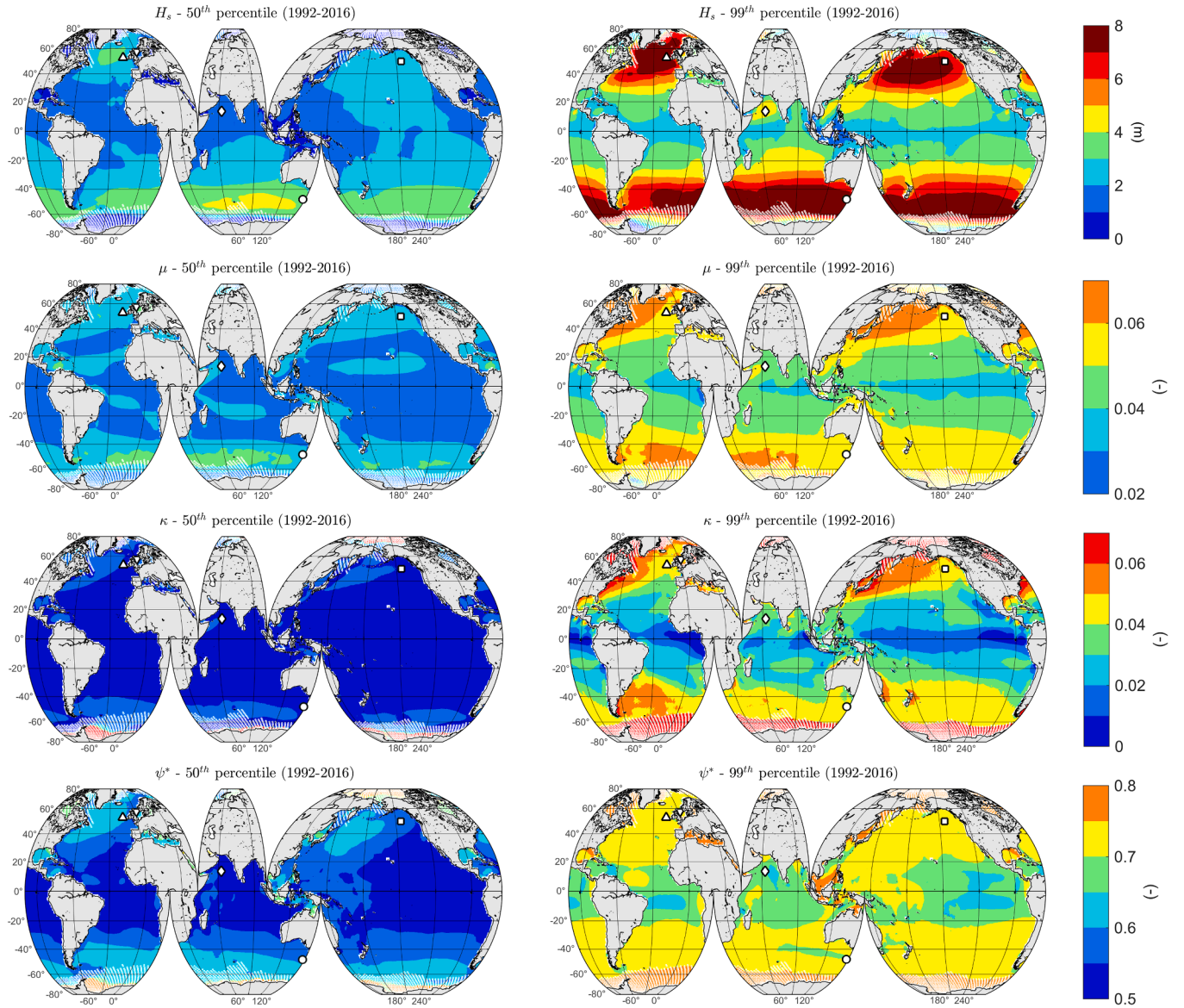
Fig. 13. Long-term global assessment of the single-point $\overline{E}_{max}$ (20 min) from EI. The white dots close to the poles indicate locations where there is lack of wave spectra, e.g., due to seasonal ice coverage.
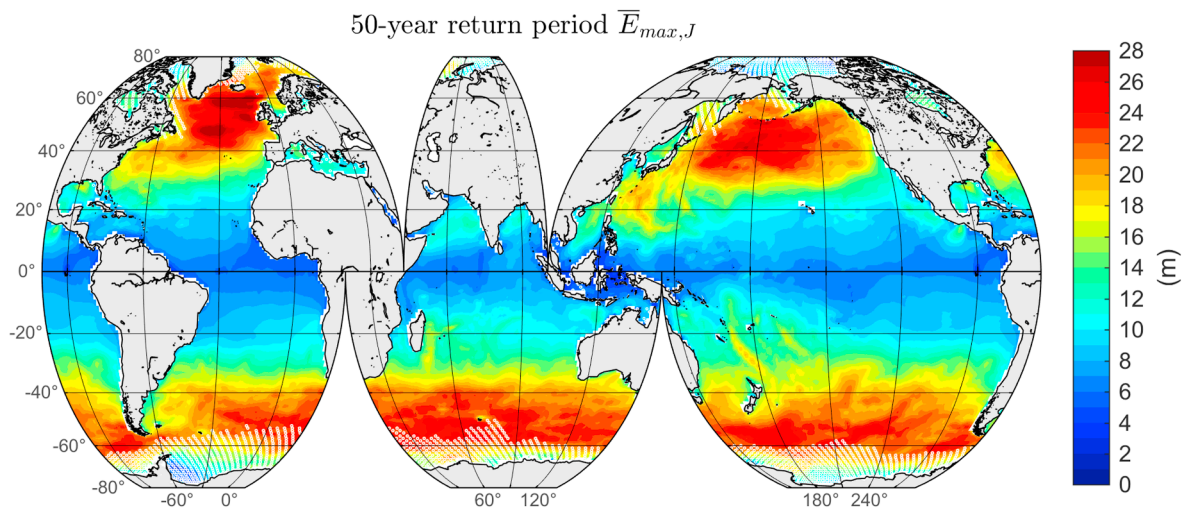
Fig. 14. Long-term global assessment of the single-point (20 min) $\overline{E}_{max}$ with return period R = 50 years from EI. The white dots close to the poles indicate locations where there is lack of wave spectra, e.g., due to seasonal ice coverage.

Fig. 15. Long-term global assessment of spectral wave parameters from EI: H_s (top panels), μ (top-middle panels), κ (bottom-middle panels) and ψ^* (bottom panels). The white dots indicate locations where, temporarily, there is lack of wave spectra, e.g., due to seasonal ice coverage. Five locations of interest are represented by black/white markers: Ocean Weather Station Papa (North Pacific, square), Southern Ocean Fluxes Station (South Pacific, circle), Draupner platform (North Sea, down-warding triangle), M6 buoy (North Atlantic, up-warding triangle), Arabian Sea (diamond).

characterized by narrower spectra, with larger values of ψ^* with respect to the equatorial regions where the superposition of wind and swell seas produce wider spectra (smaller ψ^*). This is even clearer in the inner and enclosed seas (e.g., the Mediterranean Sea) that, being dominated by wind seas rather than by combination of wind seas and swells (Cavaleri et al., 2018), present the largest μ, κ and ψ^* values. It is worth noting that globally there are vast areas with comparable H_s, but different μ, κ and ψ^*. In Section 4 we have shown that they are responsible for different $\overline{C}_{max}$, $\overline{H}_{max}$ and $\overline{E}_{max}$ for instance between North Atlantic and North Pacific.

However, maximum wave height estimates in the enclosed or semi-enclosed basins, as the Mediterranean, Baltic and Red Seas, must be carefully interpreted. Indeed, the resolution of EI winds and waves are probably too small to well represent such small, often elongated, basins. In any case, some typical wave patterns can be identified as well, for instance the high Mistral waves in the western Mediterranean Sea that can be recognized in the 99th percentile panels of all the Figures of

Section 4 and of Fig. 15.

Not being possible to describe the climate features of all the global oceans in details, we first focus our attention on three meridional (i.e., North-South) transects over the three major oceans: Atlantic Ocean (30°W), Indian Ocean (90°E), Pacific Ocean (180°E). Time extreme transects are shown in Fig. 16, those of space-time extremes in Fig. 17.

The meridional transects of the maximum wave heights are almost symmetric about the equator, with the only exception of the Indian Ocean that is mostly located in the austral hemisphere. Actually, the distributions of wave maxima in the Pacific and Atlantic oceans, at the mid latitudes (where larger values occurs) differ from the boreal to the austral hemispheres. Indeed, Pacific Ocean has larger 50th percentiles (i.e., typical values) in the austral hemisphere, while Atlantic Ocean has larger 99th percentiles and 50-year return period (i.e., extreme) values in the boreal hemisphere, in agreement with recent studies on extreme significant wave height over the globe (Breivik et al., 2014; Meucci et al., 2018; Takbash et al., 2019). Also, transects help appreciating the
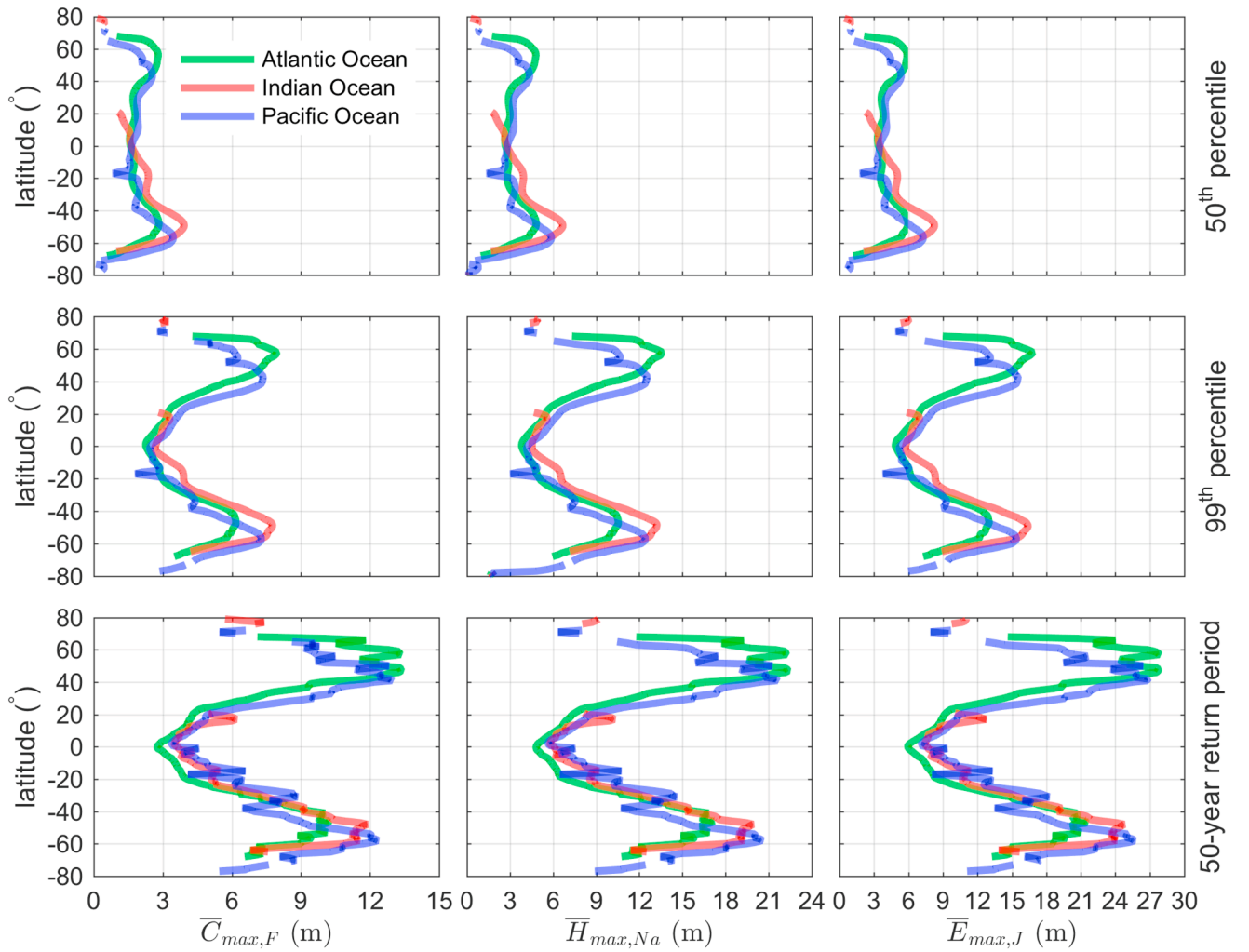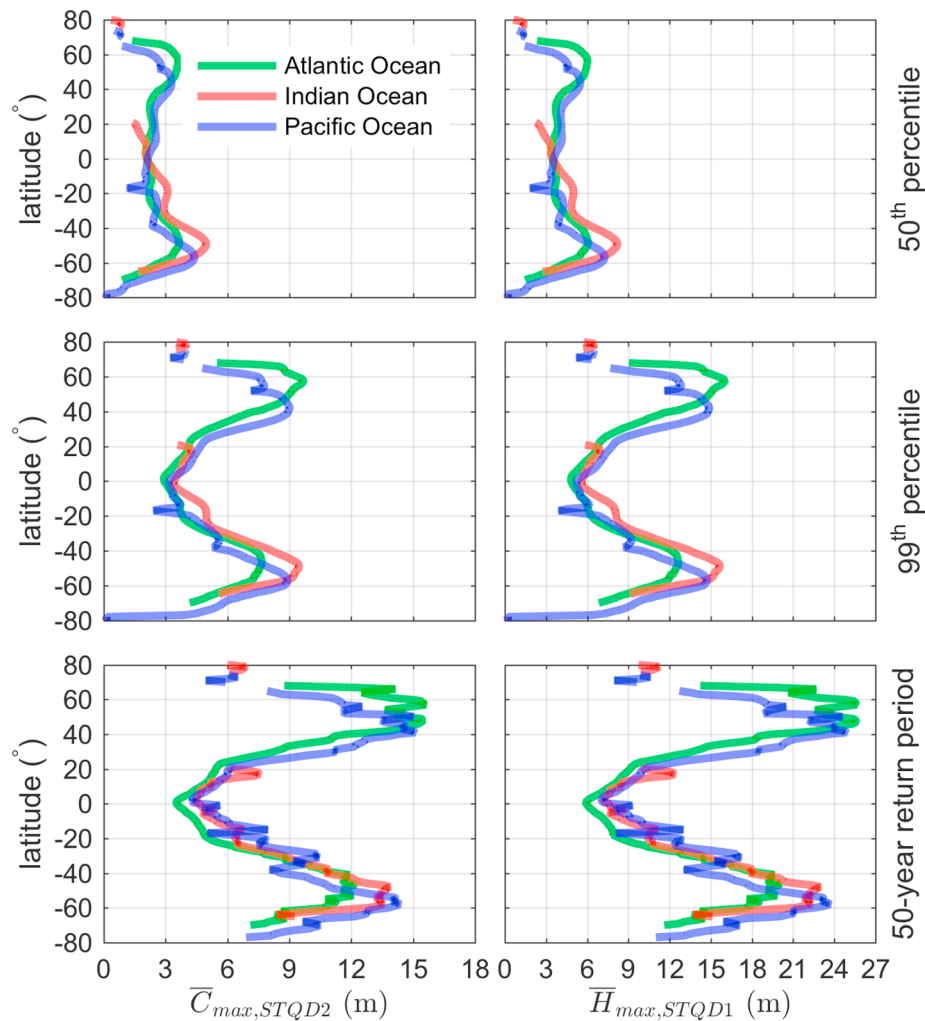
Fig. 16. Meridional transects of the time extreme $\overline{C}_{max,F}$ (left panels), $\overline{H}_{max,Na}$ (middle panels) and $\overline{E}_{max,J}$ (right panels) over the three major oceans: Atlantic Ocean (30°W), Indian Ocean (90°E), Pacific Ocean (180°E). 50th percentiles are shown in the top panels, 99th percentiles in the middle panels and 50-year return period values in the bottom panels.

larger variability of the mid latitudes with respect to equatorial zone. Indeed, differences between 50th and 99th percentiles (or 50-year return values) are very small at the equator, while can be very large elsewhere, particularly between 40° and 60° (N or S).

We now focus on five specific locations (Table 3): one in the North Pacific (Ocean Weather Station Papa, OWS-P), one in South Pacific (Southern Ocean Fluxes Station, SOFS), one in the North Sea (Draupner platform, DRAUP), one in North Atlantic (M6 buoy, M6), one in the Arabian Sea (AS). For each location, the closest EI grid point has been chosen. The first four locations represent well-known stations experiencing rough sea conditions, while the last one has been chosen as a remarkable example of a seasonal climate alternating mild and severe conditions (the latters during summer and winter Monsoons). The distribution of maximum wave heights is represented using the probability density functions (pdfs) of $\overline{C}_{max}$ and $\overline{H}_{max}$, plotted in Fig. 18. We focus on those variables only (excluding $\overline{E}_{max}$) in order to discuss the space-time to time differences. The ratio between space-time and time extremes ranges between 1.14 and 1.40, with larger ratios for 50th percentiles than for 99th percentiles, indicating that the difference from space-time to time estimates reduces for the most intense events. This effect can be ascribed to the choice of a fixed size (100×100 m^2) area

for the space-time extreme analysis: indeed, extreme conditions (i.e., 99th percentile and 50-year return period) are associated to longer wavelengths with respect to typical conditions (i.e., 50th percentile), which implies that over a space domain of fixed size the average number of waves is smaller, so the contribution of the 3D geometry of waves and short-crestedness is statistically less effective. M6 and SOFS hold the largest time extremes, but if SOFS has the largest 50th percentiles of $\overline{C}_{max}$ and $\overline{H}_{max}$ (2.91 and 4.94 m, respectively), M6 has the largest 99th percentiles (7.62 and 12.85 m, respectively), in agreement with transects in Fig. 16. The situation does not change for space-time extremes, SOFS holding the largest 50th percentile of $\overline{C}_{max}$ and $\overline{H}_{max}$ (3.98 and 6.57 m, respectively), and M6 the largest 99th percentiles (8.98 and 14.65 m, respectively), in agreement with transects in Fig. 17. The smallest values are at AS, where however the 99th to 50th percentiles ratios are the largest, with values between 3.0 and 3.4. At SOFS, instead, 99th percentiles are only 2.0–2.3 times larger than 50th percentiles. These differences in the 99th to 50th percentile ratios highlight the different persistence of large crest and crest-to-trough heights in regions with different climatic patterns, e.g. the ceaselessly rough Southern Ocean on one hand and the mild, but periodically rough, equatorial regions on the other one.

Fig. 17. Meridional transects of the space-time extreme $\overline{C}_{max,STQD2}$ (left panels) and $\overline{H}_{max,STQD1}$ (right panels) over the three oceans: Atlantic Ocean (30°W), Indian Ocean (90°E), Pacific Ocean (180°E). 50th percentiles are shown in the top panels, 99th percentiles in the middle panels and 50-year return period values in the bottom panels.

Table 3
Station list and coordinates. Longitude and latitude have been rounded to the closest integers to match the EI grid with 1.00° × 1.00° resolution.

Station	Ocean/Sea	Longitude (°E)	Latitude (°N)
Ocean Weather Station Papa (OWS-P)	North Pacific	−145	50
Southern Ocean Fluxes Station (SOFS)	South Pacific	142	−47
Draupner Platform (DRAUP)	North Sea	2	58
M6 buoy (M6)	North Atlantic	−16	53
Arabian Sea (AS)	Arabian Sea	62	14

In Fig. 18, log-normal pdfs are also fitted to the empirical functions. As we can see, excluding AS, the empirical pdfs are fairly described (well over the 99th percentiles) by the log-normal distribution, in particular for DRAUP and SOFS. This supports, in general, the choice of the Gumbel double-exponential distribution to extrapolate the $\overline{C}_{max}$ and $\overline{H}_{max}$ with 50-year return period. For AS, as well as for all the regions where there is a strong seasonality in the wave climate, the fitting has to be carefully used.

6. Summary and conclusions

In this paper we have assessed the climate of maximum wave crest, crest-to-trough and envelope heights over the global oceans, using the 25-year long ERA-Interim dataset of directional wave spectra. We have followed two different approaches that provide quantification of the time extremes (according to the Forristall, Naess and Janssen models) and of the space-time extremes (following the Space-Time Quasi
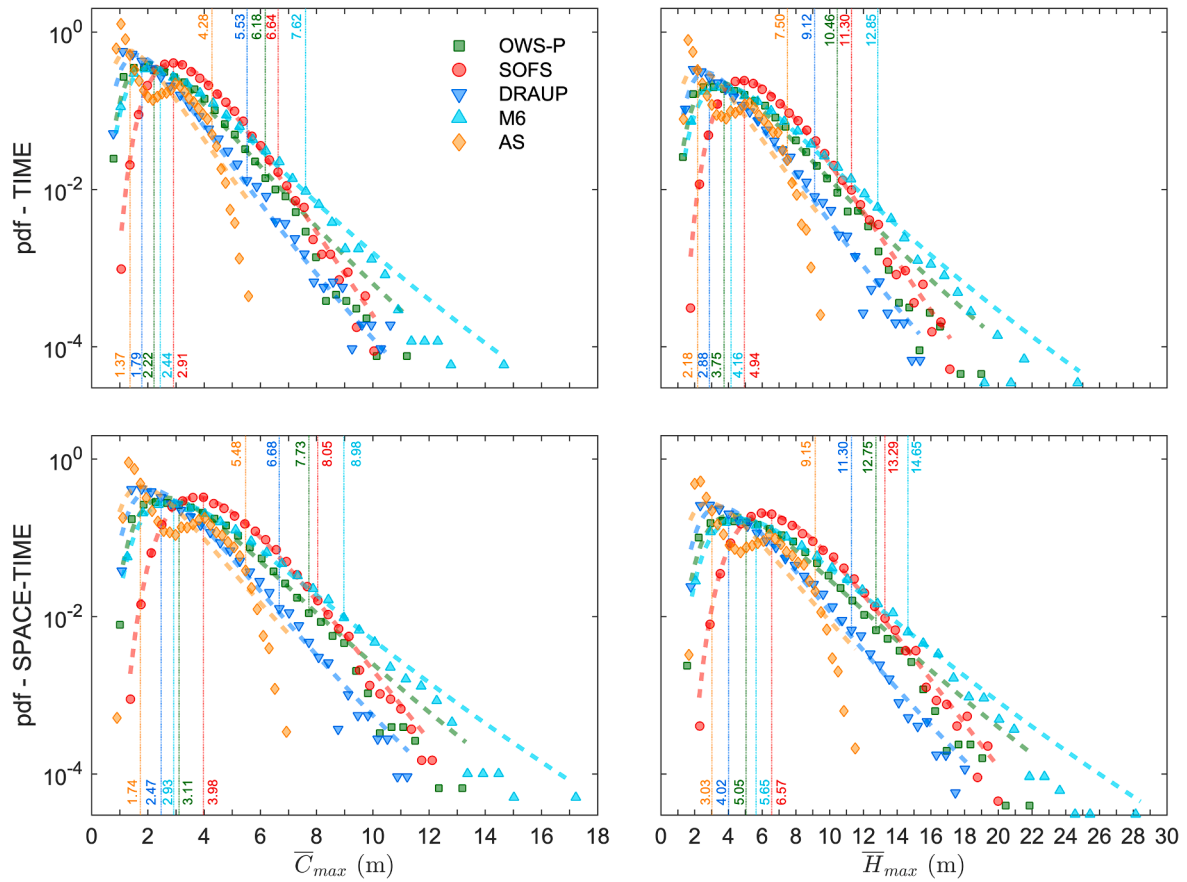
Fig. 18. Probability density functions (pdf) of time (top panels) and space-time (bottom panels) $\overline{C}_{max}$ (left panels) and $\overline{H}_{max}$ (right panels) at the five different locations of Fig. 15: OWS-P (Ocean Weather Station Papa, North Pacific), SOFS (Southern Ocean Fluxes Station, South Pacific), DRAUP (Draupner platform, North Sea), M6 (M6 buoy, North Atlantic), AS (Arabian Sea). Markers represent pdfs from numerical model data; dashed lines are the log-normal distribution that fit to data (parameters estimated with maximum likelihood). 50th and 99th percentile values are reported at the bottom and at the top of each panel, respectively.

Determinism theory). The former represent wave maxima as observed by a single-point instrument (e.g., a wave buoy or a radar altimeter), therefore we have estimated maximum wave heights over the 20-min duration, which is routinely used for buoy observations. The latter represent wave maxima as observed by an areal instrument (e.g., stereo imagery, X-band radar) or as experienced by a structure occupying a spatial extent that we have fixed equal to $100 \times 100\,m^2$ to represent an offshore rig size. We have adopted a second order nonlinear model to estimate crest heights, a linear model for crest-to-trough heights, which are only slightly affected by nonlinearities, and a third-order nonlinear model for envelope heights. Before presenting the global estimates of maximum wave heights, we have verified them against open ocean observations at the OWS-P in the North Pacific Ocean (buoy data for time extremes, stereo-video data from a vessel for space-time extremes), allowing the assessment of the accuracy of our estimates. The effect of spatio-temporal resolution of the EI spectra on the wave maxima has been also investigated comparing the EI-based estimates at OWS-P to the higher resolution E5-based estimates. For each variable, over the global oceans, we have provided the 50th percentile (the median, representing the typical value), as well as the 99th percentile (the value exceeded 1% of the times) and the 50-year return period value (representing extreme values, needed by structure designers).

We summarize our main findings in the following:

- The statistical/numerical model chain we have adopted yields fair estimates of the wave maxima at OWS-P, with statistical models (i.e., Forristall, Naess, Janssen and STQD) in very good agreement with buoy and stereo video observations, both when applied to observed and modelled spectra (12% relative difference at most). In

comparing maximum crest heights observations to both nonlinear (Forristall) and linear (Rayleigh) models, we have found evidence of the buoy linearization effect.

- The best agreement with observations at OWS-P has been obtained with E5 spectra. However, granted the minor differences between E5 and EI performance and the long-term coverage allowed by EI (25-year) at the time the study has been made, we have used EI spectra to characterize the long-term global features of the wave maxima.

- We have focused on the three major world oceans, finding, as expected, that the regions with the largest maximum crest, crest-to-trough and envelope height values are located at the mid latitudes, in the storm belts dominated by the westerlies. In the austral hemisphere, characterized by the largest 50th percentiles, large waves persist for most of the year, also favoured by the uninterrupted circular path north of Antarctica. On the contrary, the boreal hemisphere presents the largest 99th percentiles and 50-year return period values, reaching the maximal values in the North Atlantic Ocean. We have also pointed out that there are other regions, in the intra-tropical zone, that can occasionally experience large values. Assessing the climate of these regions (e.g., the Arabian Sea), rather different with respect to that of the mid-latitudes in being characterized by a strong seasonality, needs particular attention.

- Although we have verified that the global spatial patterns of extreme waves reflect the distribution of the significant wave height, we have shown that there are wave parameters that locally influence the maximum wave heights, in particular the wave steepness and kurtosis (measures of the sea state nonlinearity) and the

minimum of the autocovariance function (a measure of the spectral bandwidth, hence of the irregularity). Besides, with respect to previous studies providing wave climate features of the significant wave height (including extremes), in this paper we have provided for the first time a global quantitative assessment of maximum crest, crest-to-trough and envelope heights.

- A distinctive feature of this study is the assessment of both time and space-time extremes. We have found that the contribution of the 3D geometry and of the short-crestedness of ocean waves (taken into account by the STQD model), evaluated over a $100 \times 100 \, \text{m}^2$, is not negligible and, over a fixed size area, it is the larger the less extreme conditions are. This may have important consequences on the ship routing and the safety of navigation, but also on the design of marine structures, given, for instance, the 20% average difference between the space-time and the time 50-year return period maximum crest-to-trough heights (even larger for smaller percentiles).

Further developments are expected using the recently distributed E5 (from 1979) or other high-resolution reanalysis datasets when they will become available, in order to fill the gaps that, although small, we have observed between EI- and E5-based estimates and extend the analyses to smaller basins. Beside this, once a consensus on the climate trend existence will be reached, the contribution of a non-stationary climate may be also taken into account.

Appendix A. Theoretical statistical models for wave extremes

In this Appendix A, we describe the statistical models for maximum wave heights used in this study. To estimate the wave parameters we rely on the *ijl*-moments m_{ijl} of the directional wave spectrum $S(\omega, \theta)$:

$$m_{ijl} = \iint k_x^i k_y^j \omega^l S(\omega, \theta) d\theta d\omega$$

where ω and θ are intrinsic angular wave frequency and wave direction, (k_x, k_y) are the components of the wavenumber vector $\mathbf{k}$ in the East and North directions, respectively, and no contribution from a diagnostic spectral tail after maximum frequency is taken into account for integration.

The model for the maximum crest heights C at a single point (time extreme) is based on the nonlinear distribution of Forristall (2000):

$$P_F(C > c) = \exp\left[-\left(\frac{1}{4\alpha_F}\frac{c}{\sigma}\right)^{\beta_F}\right] \tag{1}$$

with $4\alpha_F\sigma$ providing the scaling ($\sigma = \sqrt{m_{000}}$ being the sea surface elevation standard deviation) and β_F the shape of the distribution. It accounts for the effects of second-order bound nonlinearities of the sea surface on the crest heights by means of the steepness parameter $S = 2\pi H_s(gT_1^2)^{-1}$ and the Ursell number $Ur = H_s(k_1^2 d^3)^{-1}$, which enter the distribution coefficients α_F and β_F, as follows:

$$\alpha_F = 0.3536 + 0.2568S + 0.0800Ur$$

$$\beta_F = 2 - 1.7912S - 0.5302Ur + 0.284Ur^2$$

(here, $H_s = 4\sqrt{m_{000}}$ is significant wave height, g is gravitational acceleration, $T_1 = 2\pi m_{000} m_{001}^{-1}$ is spectral mean wave period, k_1 is the deep-water mean wavenumber for a frequency T_1^{-1}, and d is water depth). Coefficients of the Forristall distribution result from empirical fittings of 2D (long-crested) and 3D (short-crested) numerical simulations. In this study, we have chosen the 3D version as we assume that the typical oceanic conditions, especially during storms, are short-crested (Benetazzo et al., 2015; Fedele et al., 2013). For zero steepness and Ursell number, effects of nonlinearity vanish and coefficients revert to Rayleigh values ($\alpha = 1/\sqrt{8}$, $\beta = 2$). Following Goda (2000), the probability of the maximum crest height in a sea state with an average number of waves N can be expressed as $P(C_{max,F} > c) = P_F^N$, which, for large values of c and N, is in turn fairly well approximated by a double exponential Gumbel-type distribution. This allows computing the expected value of the maximum crest height at a single-point, as:

$$\overline{C}_{max,F} = 4\sigma\alpha_F(\ln N)^{1/\beta_F}\left(1 + \frac{\gamma}{\beta_F \ln N}\right) \tag{2}$$

being $\gamma \approx 0.5772$ the Euler-Mascheroni constant. The average number of waves can be estimated as $N = DT_z^{-1}$, being D the duration of the sea state (from few tenths of minutes to few hours) and T_z the average zero-crossing wave period, fairly well approximated by the spectral mean period $T_2 = 2\pi\sqrt{m_{000} m_{002}^{-1}}$.

The model for the maximum crest-to-trough height H at a point (time extreme) is based on the Naess (1985) distribution of crest-to-trough heights: a Rayleigh-like distribution (i.e., the shape parameter is equal to 2) that generalizes the Rayleigh one to account for arbitrary spectral bandwidth effects on the wave heights:

$$P_{Na}(H > h) = \exp\left[-\frac{1}{4(1 - \psi^*)}\left(\frac{h}{\sigma}\right)^2\right] \tag{3}$$

being ψ^* a bandwidth parameter, which in typical wind-sea conditions assumes values in the $[-0.75, -0.65]$ range. This decreases the probability with respect to Rayleigh (recovered for $\psi^* = -1$), which represents an upper bound. Among the various interpretations on how to estimate ψ^*, we rely on that of Boccotti (2000) who defined ψ^* as the minimum of the autocovariance function of the sea surface elevation $\psi(t)$, which can be estimated from the directional spectrum as:

$$\psi(t) = \frac{1}{\sigma^2} \int \int S(\omega, \theta) d\theta \cos(\omega t) d\omega \tag{4}$$

The probability of the maximum wave height in a sea state with N waves can be expressed as $P(H_{max,Na} > h) = P_F^N$, and for large values of h and N the Gumbel-type approximation provides the expected value of the maximum wave height at a single-point, that is:

$$\overline{H}_{max,Na} = 2\sigma\sqrt{1 - \psi^*}(\ln N)^{1/2}\left(1 + \frac{\gamma}{2\ln N}\right) \tag{5}$$

The same expression can be obtained using the Quasi-Determinism theory of Boccotti (2000), that is, scaling the deterministic shape of the highest waves (represented by the autocovariance function) with the expected value of the maximum linear crest height at a point. Indeed, the distribution of Boccotti is consistent with that of Naess, except for being an asymptotic distribution, i.e., it holds for large values of h and it is not normalized to 1 at $h = 0$.

The model for the maximum envelope heights E at a point (time extremes) is based on the approach proposed by Janssen (2003) and further developed by Janssen (2014) who presented a general framework relating the shape of the probability distribution function (pdf) of the surface elevation to the mean sea state as described by the two-dimensional frequency spectrum. In so doing, although the estimate is actually in the time domain, the width of the directional distribution, hence the short-crestedness, is taken into account. Deviations from the normality of the probability distribution (otherwise Gaussian) occur when the spectrum is narrow both in frequency and direction, and are measured in terms of the kurtosis κ and skewness λ of the sea surface elevation (Janssen, 2014), such that the parent pdf of E is:

$$p(EH_s^{-1}) = 4EH_s^{-1}e^{-2E^2H_s^{-2}}\{1 + \kappa(2E^4H_s^{-4} - 4E^2H_s^{-2} + 1) + \lambda^2(4E^6H_s^{-6} - 18E^4H_s^{-4} + 18E^2H_s^{-2} - 3)\} \tag{6}$$

Kurtosis κ and skewness λ contemplate the nonlinear contributions from both free and bound waves and are estimated from the spectrum as:

$$\kappa = \kappa^{free} + \kappa^{bound}$$

$$\lambda = \lambda^{bound}$$

where the effect of free waves on the skewness has been neglected being very small. In the narrow-banded approximation κ^{free} depends on the Benjamin-Feir Index (BFI) and the spectral widths in frequency δ_ω and direction δ_θ, with correction for shallow-water effects. The former is computed as $BFI = \sqrt{2} \epsilon \delta_\omega^{-1}$ (with $\epsilon = k_p\sqrt{m_{000}}$ the integral wave steepness based on the peak wavenumber k_p), while the latters are estimated from a two-dimensional parabolic fitting around the peak of the spectrum. κ^{bound} and λ^{bound} solely depend on the integral steepness ϵ. A detailed description of how λ and κ are computed by the ECMWF wave model and how they have been computed in this paper can be found in the Integrated Forecasting System documentation, cycle Cy43r3 (ECMWF, 2017; chapter 10).

The expected maximum envelope height at a single point $\overline{E}_{max}$ is obtained integrating the probability distribution $P(E_{max} > e)$, derived from the parent distribution in Eq. (6) following the Goda (2000) approach. It is:

$$\overline{E}_{max} = \left\{\sqrt{z_0} + \frac{1}{4\sqrt{z_0}}[\gamma + \ln(1 + \widehat{\alpha}\kappa + \widehat{\beta}\lambda^2)]\right\}H_s$$

where $z_0 = 0.5\ln(N)$ and the expressions for $\widehat{\alpha}$ and $\widehat{\beta}$ can be found in ECMWF (2017; chapter 10). The average number of independent wave groups N_G in a time series of length D is computed as:

$$N_G = \frac{2E_c}{\sqrt{2\pi}}\upsilon\omega_m D$$

where $\omega_m = m_{001}m_{000}^{-1}$ is the mean wave frequency, $\upsilon = \sqrt{m_{000}m_{002}m_{001}^{-2} - 1}$ is the spectral bandwidth parameter (Longuet-Higgins, 1975) and $E_c = \sqrt{2}$ is a reference value.

Space-time extreme crest and crest-to-trough heights are modelled in the framework of the Space-Time Quasi Determinism theory (Benetazzo et al., 2015; Benetazzo et al., 2017; Boccotti, 2000; Fedele, 2012). In this context, the probability for the maximum crest height $C_{max,STQD2}$ of exceeding a threshold c over an area XY and in a duration D is expressed as (Benetazzo et al., 2015):

$$P(C_{max,STQD2} > c) = \left(N_3\frac{c_0^2}{\sigma^2} + N_2\frac{c_0}{\sigma} + N_1\right)\exp\left(-\frac{c_0^2}{2\sigma^2}\right) \tag{7}$$

with $c_0 = \sigma(-1 + \sqrt{1 + 2\mu c\sigma^{-1}})\mu^{-1}$, relating the first ($c_0$) and the second ($c$) order thresholds as a function of μ (Fedele and Tayfun, 2009; Tayfun, 1980), which is proportional to skewness ($\mu = \lambda/3$) and measures the contribution of the second order nonlinearities. An integral measure of μ in deep waters (a fair approximation for our global analysis) that accounts for bandwidth effects has been proposed by Fedele and Tayfun (2009) as:

$$\mu = \mu_m(1 - \upsilon + \upsilon^2) \tag{8}$$

with $\mu_m = \sigma\omega_m^2 g^{-1}$ the narrow-banded wave steepness. It allows for the computation of μ from the directional spectrum and its integral parameters, like the standard deviation of the sea surface elevation σ, the mean wave frequency ω_m, and the spectral bandwidth parameter υ. The probability in Eq. (7) is the sum of the contributions of 3D waves in the space-time volume XYD (first term), of 2D waves on its faces (second term) and 1D waves on its boundaries (third term). The second and the third terms are significant, but determinant only when the area is small ($XY < L_x L_y$, where $L_x = 2\pi\sqrt{m_{000}m_{200}^{-1}}$ and $L_y = 2\pi\sqrt{m_{000}m_{020}^{-1}}$ are the East and North components of mean wavelength, respectively, which correspond to mean wave length and mean wave crest length if direction θ is referred to the dominant wave direction). In analogy with the single-point time model, in the space-time model the average numbers of waves are computed as the domain size to characteristic wave size ratio, in particular:

$$N_{3D} = \frac{N_3}{2\pi} = \frac{XYD}{L_x L_y T_2}\sqrt{1 - \alpha_{xt}^2 - \alpha_{xy}^2 - \alpha_{yt}^2 + 2\alpha_{xt}\alpha_{xy}\alpha_{yt}}$$

$$N_{2D} = \frac{N_2}{\sqrt{2\pi}} = \frac{XD}{L_x T_2}\sqrt{1 - \alpha_{xt}^2} + \frac{YD}{L_y T_2}\sqrt{1 - \alpha_{yt}^2} + \frac{XY}{L_x L_y}\sqrt{1 - \alpha_{xy}^2}$$

$$N_{1D} = N_1 = \frac{X}{L_x} + \frac{Y}{L_y} + \frac{D}{T_2}$$

$$(9)$$

Parameters $\alpha_{xt} = m_{101}(m_{200}m_{002})^{-1/2}$, $\alpha_{xy} = m_{110}(m_{200}m_{020})^{-1/2}$ and $\alpha_{yt} = m_{011}(m_{020}m_{002})^{-1/2}$ account for the correlations between space and time or space and space and reduce the number of waves accordingly, to avoid redundancies. For large crest heights, the probability distribution of Eq. (7) can be approximated by a Gumbel-type distribution, and the expected value of the maximum crest height in space and time (space-time extreme) is estimated as:

$$\bar{C}_{max,STQD2} = \xi_0 + \frac{\mu}{2}\frac{\xi_0^2}{\sigma} + \sigma\gamma\left[(1 + \mu\xi_0\sigma^{-1})\left(\xi_0\sigma^{-1} - \frac{2N_3\xi_0\sigma^{-1} + N_2}{N_3\xi_0^2\sigma^{-2} + N_2\xi_0\sigma^{-1} + N_1}\right)\right]^{-1}$$

$$(10)$$

In Eq. (10), $\xi_0\sigma^{-1}$ is the mode of the Gaussian distribution, obtained as the largest positive solution of $P(C_{max,STQD2} > c) = 1$, after setting $\mu = 0$.

Maximum crest-to-trough wave heights over a space-time region are estimated by means of the Quasi-Determinism theory, which establishes a relationship between the expected maximum crest and crest-to-trough wave heights, in the context of the deterministic behaviour of the largest waves (Boccotti, 2000). Hence, given the linear $\bar{C}_{max,STQD1}$, which is obtained from Eq. (10) by setting $\mu = 0$ and assumed to occur at a fixed point in space where a wave group reaches the apex of its development, $\bar{H}_{max,STQD1}$ (space-time extreme) is:

$$\bar{H}_{max,STQD1} = \left[\xi_0 + \sigma\gamma\left(\xi_0\sigma^{-1} - \frac{2N_3\xi_0\sigma^{-1} + N_2}{N_3\xi_0^2\sigma^{-2} + N_2\xi_0\sigma^{-1} + N_1}\right)^{-1}\right]\sqrt{2(1 - \psi^*)}$$

$$(11)$$

Appendix B. Observational data analysis

Here, we present the methodology of wave data analysis we have used with buoy and stereo data to obtain empirical estimates of the time and space-time extremes, respectively.

Buoy sea surface elevation data (June 2010–December 2014, sampled at 1.28 Hz) have been first quality checked, following the criteria used by Casas-Prat and Holthuijsen (2010). Then, the following procedure is applied:

a. the 4.5-year time series is partitioned into 3-h segments, i.e. sea states $\eta(t)$, that we assume stationary and represented by the same spectrum;
b. each sea state is further partitioned into 9 segments which represent 20-min realizations $\eta_i(t)$ of the sea state;
c. zero-crossing analysis is performed on each realization in order to extract the maximum crest C_{max_i} and crest-to-trough height H_{max_i};
d. the envelope ρ_i of each realization $\eta_i(t)$ is computed by taking the complex magnitude of the Hilbert transform of $\eta_i(t)$ and doubled to obtain the envelope height $E_i = 2\rho_i$. Then the maximum of each envelope height E_{max_i} is extracted;
e. the estimate of expected maximum crest $\overline{C}_{max}$, crest-to-trough $\overline{H}_{max}$ and envelope height $\overline{E}_{max}$ in a 20-min sea state is obtained by averaging the nine realizations of maxima.
f. $\overline{C}_{max}$, $\overline{H}_{max}$ and $\overline{E}_{max}$ have been upscaled of 2%, i.e., the sampling bias correction for the OWS-P buoy data (Tayfun, 1993).

The points a. and b. of the adopted procedure are in agreement with what done by Janssen and Bidlot (2009) to estimate the expected value of maximum wave height from buoy observations. It is worth noting that we have also repeated the analysis with a larger number of realizations (e.g., 36 of 5 min each) to verify the statistical robustness of the estimate, with comparable results.

The stereo datasets (2 events sampled at 7.5 Hz and on a 0.25 m resolution square grid) are processed in a different way. First, the sea surface elevation time series $\eta(x_j, y_l, t)$ at every point (x_j, y_l) in space is low-pass filtered at 0.8 Hz in order to remove high frequency noise and taken to null mean by subtracting the time series average. Then, the following procedure is applied:

• the observed 1000 m² wide and 30-min long space-time sea surface elevation $\eta(x, y, t)$ is partitioned into space-time sub-volumes that represent realizations of the same sea state. The space area is divided into 4 equivalent areas (size of about 15×15 m²), the duration is divided into six 5-min segments, thus generating 24 realizations;
• the maximum sea surface elevation from each realization is extracted and labelled as C_{max_i}, after verifying that they all belong to different, hence independent, waves (time between two C_{max_i} should exceed a dominant wave period T_p). If one crest is closer to another, it is discarded;
• the time series of the sea surface elevation at the positions where C_{max_i} occurred are isolated (selecting only the time series portion around C_{max_i}, i.e., $t_i \pm 1.5T_p$) and then averaged in order to obtain the mean temporal profile;
• the estimates of the expected maximum crest height $\overline{C}_{max}$ and related wave height $\overline{H}_{Cmax}$ in a 5-min sea state and over 15×15 m² are obtained as the largest crest and the largest crest-to-trough excursion of the mean temporal profile, respectively;
• no sampling bias correction has been applied to the stereo data as the sampling intervals in both space and time are small enough, compared to mean wave periods and wavelengths, to strongly reduce the wave height underestimation due to equidistant sampling (Tayfun, 1993).

We recall that envelope heights have been only estimated in the time domain.

References

Aarnes, O.J., Abdalla, S., Bidlot, J.R., Breivik, Ø., 2015. Marine wind and wave height trends at different ERA-interim forecast ranges. J. Clim. 28 (2), 819–837. https://doi.org/10.1175/JCLI-D-14-00470.1.

Adler, R.J., 1981. The Geometry of Random Fields. John Wiley & Sons, Chichester.
Adler, R.J., Taylor, J.E., 2007. Random Fields and Geometry, vol. 115 Springer.
Barbariol, F., Alves, J.-H.G.M., Benetazzo, A., Bergamasco, F., Bertotti, L., Carniel, S., Tolman, H., 2017. Numerical modeling of space-time wave extremes using WAVEWATCH III. Ocean Dyn. 67, 535–549. https://doi.org/10.1007/s10236-016-1025-0.

Barbariol, F., Benetazzo, A., Carniel, S., Sclavo, M., 2015. Space-time wave extremes: the role of metocean forcings. J. Phys. Oceanogr. 45 (7), 1897–1916. https://doi.org/10.1175/JPO-D-14-0232.1.

Benetazzo, A., Ardhuin, F., Bergamasco, F., Cavaleri, L., Veras, P., Schwendeman, M., Torsello, A., 2017a. On the shape and likelihood of oceanic rogue waves. Sci. Rep. 7 (8276), 1–11. https://doi.org/10.1038/s41598-017-07704-9.

Benetazzo, A., Barbariol, F., Bergamasco, F., Carniel, S., 2017b. Space-time extreme wind waves: analysis and prediction of shape and height. Ocean Model. 113, 201–216. https://doi.org/10.1016/j.ocemod.2017.03.010.

Benetazzo, A., Barbariol, F., Bergamasco, F., Torsello, A., Carniel, S., Sclavo, M., 2015. Observation of extreme sea waves in a space-time ensemble. J. Phys. Oceanogr. 45 (9), 2261–2275. https://doi.org/10.1175/JPO-D-15-0017.1.

Benetazzo, A., Bergamasco, F., Yoo, J., Cavaleri, L., Sun-Sin, K., Bertotti, L., Jae-Seol, S., 2018. Characterizing the signature of a spatio-temporal wind wave field. Ocean Model. 129, 104–123. https://doi.org/10.1016/j.ocemod.2018.06.007.

Boccotti, P., 2000. Wave Mechanics for Ocean Engineering, vol. 64 Elsevier Science.

Breivik, Ø., Aarnes, O.J., Abdalla, S., Bidlot, J.R., Janssen, P.A.E.M., 2014. Wind and wave extremes over the world oceans from very large ensembles. Geophys. Res. Lett. 41 (14), 5122–5131. https://doi.org/10.1002/2014GL060997.

Casas-Prat, M., Holthuijsen, L.H., 2010. Short-term statistics of waves observed in deep water. J. Geophys. Res. Oceans 1978–2012, 115(C9).

Cavaleri, L., Abdalla, S., Benetazzo, A., Bertotti, L., Bidlot, J.R., Breivik, van der Westhuysen, A.J., 2018. Wave modelling in coastal and inner seas. Prog. Oceanogr. https://doi.org/10.1016/j.pocean.2018.03.010.

Cavaleri, L., Barbariol, F., Benetazzo, A., Bertotti, L., Bidlot, J., Janssen, P.A.E.M., Wedi, N., 2016. The Draupner wave: a fresh look and the emerging view. J. Geophys. Res. – Oceans.

Cavaleri, L., Benetazzo, A., Barbariol, F., Bidlot, J., Janssen, P.A.E.M., 2017. The Draupner event: the large wave and the emerging view. Bull. Am. Meteorol. Soc. 98 (4), 729–735.

Cox, A.T., Swail, V.R., 2001. A global wave hindcast over the period 1958–1997: validation and climate assessment. J. Geophys. Res. Oceans 106 (C2), 2313–2329. https://doi.org/10.1029/2001JC000301.

Dee, D.P., Uppala, S.M., Simmons, A.J., Berrisford, P., Poli, P., Kobayashi, S., Dee, D.P., 2011. The ERA-Interim reanalysis: configuration and performance of the data assimilation system. Q. J. R. Meteorolog. Soc. 137 (April), 553–597. https://doi.org/10.1002/qj.828.

DNV GL - Det Norske Veritas Germanischer Lloyd, 2017. DNVGL-RP-C205: Environmental Conditions and Environmental Loads. DNV GL Recommended Practice (August), 1–259.

Dysthe, K., Krogstad, H.E., Müller, P., 2008. Oceanic rogue waves. Annu. Rev. Fluid Mech. 40, 287–310.

ECMWF, 2017. Part VII : ECMWF Wave Model IFS DOCUMENTATION – PART VII : ECMWF WAVE MODEL. In: IFS Documentation CY43R3. Retrieved from https://www.ecmwf.int/en/elibrary/17739-part-vii-ecmwf-wave-model. pp. 1–99.

Fedele, F., 2012. Space-time extremes in short-crested storm seas. J. Phys. Oceanogr. 42 (9), 1601–1615.

Fedele, F., 2015. On oceanic rogue waves. ArXiv:1501.03370v5. Retrieved from < http://arxiv.org/abs/1501.03370 > .

Fedele, F., Benetazzo, A., Gallego, G., Shih, P.C., Yezzi, A., Barbariol, F., Ardhuin, F., 2013. Space-time measurements of oceanic sea states. Ocean Model. 70, 103–115.

Fedele, F., Lugni, C., Chawla, A., 2017. The sinking of the El Faro: predicting real world rogue waves during Hurricane Joaquin. Sci. Rep. 7 (11188), 1–15. https://doi.org/10.1038/s41598-017-11505-5.

Fedele, F., Tayfun, M.A., 2009. On nonlinear wave groups and crest statistics. J. Fluid Mech. 620, 221–239.

Forristall, G.Z., 2000. Wave crest distributions: observations and second-order theory. J. Phys. Oceanogr. 38 (8), 1931–1943.

Forristall, G.Z., 2006. Maximum wave heights over an area and the air gap problem. In: Proc. ASME 25th Inter. Conf. Off. Mech. Arc. Eng., Hamburg, OMAE2006-92022, pp. 11–15.

Forristall, G.Z., 2011. Maximum crest heights under a model TLP deck. In: Proceedings of the ASME 2011 30th International Conference on Ocean, Offshore and Arctic

Engineering.

Goda, Y., 2000. Random Seas and Design Of Maritime Structures. World Scientific.

Gumbel, E.J., 1958. Statistics of Extremes. Columbia Univ. Press, New York.

Hersbach, H., de Rosnay, P., Bell, B., Schepers, D., Simmons, A., Soci, C., et al., 2018. Operational global reanalysis: progress, future directions and synergies with NWP. Retrieved from < https://www.ecmwf.int/node/18765 > .

Holthuijsen, L.H., 2007. Waves in Oceanic and Coastal Waters. Cambridge University Press.

Janssen, P.A.E.M., 2003. Nonlinear four-wave interactions and freak waves. J. Phys. Oceanogr. 33 (4), 863–884.

Janssen, P.A.E.M., 2014. On a random time series analysis valid for arbitrary spectral shape. J. Fluid Mech. 759, 236–256. https://doi.org/10.1017/jfm.2014.565.

Janssen, P., Bidlot, J.-R., 2009. On the extension of the freak wave warning system and its verification. Technical Memorandum. ECMWF.

Komen, G.J., Cavaleri, L., Donelan, M., Hasselmann, K., Hasselmann, S., Janssen, P.A.E.M., 1994. Dynamics and Modelling of Ocean Waves. Cambridge University Press. https://books.google.it/books?id=7sg_PN_PDUkC.

Krogstad, H.E., Liu, J., Socquet-Juglard, H., Dysthe, K.B., Trulsen, K., 2004. Spatial extreme value analysis of nonlinear simulations of random surface waves. In: Proceedings of the ASME 2004 23rd International Conference on Ocean, Offshore and Arctic Engineering.

Longuet-Higgins, M.S., 1975. On the joint distribution of the periods and amplitudes of sea waves. J. Geophys. Res. 80 (18), 2688–2694.

Meucci, A., Young, I.R., Breivik, Ø., 2018. Wind and wave extremes from atmosphere and wave model ensembles. J. Clim. 31 (21), 8819–8842. https://doi.org/10.1175/JCLI-D-18-0217.1.

Naess, A., 1985. On the distribution of crest to trough wave heights. Ocean Eng. 12 (3), 221–234. https://doi.org/10.1016/0029-8018(85)90014-9.

Piterbarg, V.I., 1996. Asymptotic Methods in the Theory of Gaussian Processes and Fields. AMS Transl. of Math Monographs.

Schwendeman, M.S., Thomson, J., 2017. Sharp-crested breaking surface waves observed from a ship-based stereo video system. J. Phys. Oceanogr. 47 (4), 775–792. https://doi.org/10.1175/JPO-D-16-0187.1.

Socquet-Juglard, H., Dysthe, K., Trulsen, K., Krogstad, H.E., Liu, J., 2005. Probability distributions of surface gravity waves during spectral changes. J. Fluid Mech. 542 (1), 195–216.

Stopa, J.E., Cheung, K.F., 2014a. Intercomparison of wind and wave data from the ECMWF Reanalysis Interim and the NCEP Climate Forecast System Reanalysis. Ocean Model. 75, 65–83. https://doi.org/10.1016/j.ocemod.2013.12.006.

Stopa, J.E., Cheung, K.F., 2014b. Periodicity and patterns of ocean wind and wave climate. J. Geophys. Res. Oceans 119, 2121–2128. https://doi.org/10.1002/jgrc.20224.

Takbash, A., Young, I.R., Breivik, Ø., 2019. Global wind speed and wave height extremes derived from long-duration satellite records. J. Clim. 32 (1), 109–126. https://doi.org/10.1175/JCLI-D-18-0520.1.

Tayfun, M.A., 1980. Narrow-band nonlinear sea waves. J. Geophys. Res. 85 (C3), 1548–1552.

Tayfun, M.A., 1993. Sampling-rate errors in statistics of wave heights and periods. J. Waterw. Port Coastal Ocean Eng. https://doi.org/10.1061/(ASCE)0733-950X(1993) 119:2(172).

Tayfun, M.A., Fedele, F., 2007. Wave-height distributions and nonlinear effects. Ocean Eng. 34, 1631–1649.

The WAVEWATCH III Development Group (WW3DG), 2016. User manual and system documentation of WAVEWATCH III-version 5.16. College Park, MD, USA.

Thomson, J.A., D'Asaro, A., Cronin, F., Rogers, E., Harcourt, R., Shcherbina, A., 2013. Waves and the equilibrium range at Ocean Weather Station P. J. Geophys. Res. Oceans 118 (11), 5951–5962. https://doi.org/10.1002/2013JC008837.

Young, I.R., 1999. Wind Generated Ocean Waves, vol. 2 Elsevier Science Limited.

Young, I.R., Vinoth, J., Zieger, S., Babanin, a.V., 2012. Investigation of trends in extreme value wave height and wind speed. J. Geophys. Res. 117 (November 2011), C00J06. https://doi.org/10.1029/2011JC007753.

Young, I.R., Zieger, S., Babanin, A.V., 2011. Global trends in wind speed and wave height. Science 159 (April), 451–455.